

MEDIATED ELECTROCHEMICAL REDUCTION: A CONTROL FOR  
ELECTRON TRANSFER REACTIONS AND IMPLICATIONS FOR REDOX  
CYCLING OF IRON AND PHOSPHORUS BETWEEN SEDIMENT AND WATER

Natalie A. Maag

Submitted to the faculty of the University Graduate School  
in partial fulfillment of the requirements  
for the degree  
Master of Science  
in the Department of Earth Sciences,  
Indiana University

May 2025

Accepted by the Graduate Faculty of Indiana University, in partial fulfillment of the requirements for the degree of Master of Science.

Master's Thesis Committee

Gregory K. Druschel, Ph. D., Chair

Gabriel M. Filippelli, Ph. D.

Frédérique Deiss, Ph. D.

© 2025  
Natalie A. Maag

## DEDICATION

The work of this thesis is largely dedicated to my husband, Ethan Maag, who has unconditionally supported me through my undergraduate and graduate school journeys, and beyond.

## ACKNOWLEDGEMENTS

My list of acknowledgements begins with my family. My parents, John and Rhonda Nichols, my sister, Ashley Sanders, my husband, Ethan Maag, my grandparents and in-laws have always uplifted me and pushed me to succeed. Without them I would lack people to laugh with during our memorable times together, and in some instances, shoulders to cry on in the face of challenges. Their endless support has never gone unnoticed.

I would also like to acknowledge the IU(PU)I Earth Science Department as a whole, and specifically my advisor Greg Druschel, for helping me grow as a student, teaching assistant, researcher, and scientist. Being my home for seven years, this department has given me so many opportunities that I never would have pictured for myself. From field trips and trips to California to do research, to friends, to mentors, it never ceases to amaze me what things I could accomplish with the support I have from the faculty and peers. Our collaborators, including Martin Kurek and Jocelyn Richardson have provided me with knowledge and guidance in our electroanalytical techniques and beamline data analysis that helped to make this research possible.

I would lastly like to thank all of the friends I made in graduate school, including Lynn Thomas, Spencer Strout, John Shukle, Kate Hostetler, Kiersten LaRoche, Raenah Bailey, Alex Horman, David Wallington, Brooke Vander Pas, and so many more that made the journey so much more enjoyable with them than without them. Many cheers and thanks to all those who have been there along the way.

Natalie A. Maag

MEDIATED ELECTROCHEMICAL REDUCTION: A CONTROL FOR  
ELECTRON TRANSFER REACTIONS AND IMPLICATIONS FOR REDOX  
CYCLING OF IRON AND PHOSPHORUS BETWEEN SEDIMENT AND WATER

Eutrophication of terrestrial lacustrine systems is an ongoing environmental issue that has grown more troublesome in recent years due to continuous historic loading of phosphorus in these systems. A major hurdle for estimating phosphorus loading in lakes arises from the difficulties in determining internal loading mechanisms that release phosphorus from iron-rich sediments during reducing conditions, driven by stable hydrodynamic conditions that occur typically during colder months. Using mediated electrochemical reduction techniques to drive reduction in experimental sediment systems representing those near the sediment water interface, we found that both iron and phosphorus are released from sediments, however subsequent aqueous geochemical analysis of the system does not account for all the iron and phosphorus in the initial sediment sample. With natural sediment samples obtained from Missisquoi Bay, Lake Champlain, Vermont, iron and phosphorus released from sediments after reduction continued to increase with increasing sediment samples. Further experimentation with phosphate-sorbed ferrihydrite and goethite samples resulted in aqueous solution saturation of these components, and loss of these components in the aqueous phase likely as a result of reprecipitation of iron-phosphate mineral precipitation. Increasing phosphate in solution also significantly decreased the reduction extents and rates of phosphate-sorbed ferrihydrite minerals, indicating that phosphate sorption may create a shielding effect of these minerals and prevent electron transfer at surface sites.

Gregory K. Druschel, Ph. D., Chair

Gabriel M. Filippelli, Ph. D.

Frédérique Deiss, Ph. D.

## TABLE OF CONTENTS

|  |      |
|--|------|
| List of Tables .....   | viii |
| List of Figures .....  | ix   |
| List of Abbreviations .....  | xi   |
| Chapter One: A Review of Relevant Literature and Overview of Experimental<br>Techniques .....                                  | 1    |
| 1.1 Introduction .....   | 1    |
| 1.1.1 Motivation .....   | 1    |
| 1.1.2 Hypothesis and Research Questions .....  | 1    |
| 1.2 Literature Review .....  | 2    |
| 1.2.1 Phosphorus in Our Environment: Nutrient and Contaminant .....  | 2    |
| 1.2.2 Internal Loading of P in Terrestrial Aquatic Systems .....   | 5    |
| 1.2.3 Oxidizing Conditions .....   | 6    |
| 1.2.4 Reducing Conditions .....  | 7    |
| 1.2.5 Coupled Redox Cycling and Algal Blooms .....   | 9    |
| 1.2.6 Mediated Electrochemical Approaches to Control Redox Reactions .....   | 10   |
| 1.3 Experimental Overview .....  | 12   |
| 1.3.1 Mediated Electrochemical Techniques .....  | 12   |
| 1.3.2 $\mu$ -X-Ray Fluorescence (Multi-)Energy Mapping .....   | 13   |
| 1.3.3 X-Ray Absorption Near-Edge Structure Spectroscopy .....  | 14   |
| Chapter Two: Mediated Electrochemical Reduction as a Tool to Characterize P and Fe<br>Cycling Between Sediment and Water ..... | 15   |
| 2.1 Introduction .....   | 15   |
| 2.2 Methods .....  | 19   |
| 2.2.1 Mediated Electrochemical Reduction and Oxidation Experiments .....   | 19   |
| 2.2.2 Phosphate Sorption Experiments .....   | 20   |
| 2.2.3 Spectrophotometry Techniques .....   | 21   |
| 2.2.4 $\mu$ -X-Ray Fluorescence (Multi)Energy Mapping .....  | 21   |
| 2.2.5 X-Ray Absorption Near-Edges Spectroscopy Spot Analyses .....   | 23   |
| 2.3 Results .....  | 23   |
| 2.3.1 Mediated Electrochemical Reduction and Oxidation of MBS Samples .....  | 23   |
| 2.3.2 Total Dissolved Iron and Soluble Reactive Phosphate from MBS .....   | 26   |
| 2.3.3 Mediated Electrochemical Reduction of Pure Mineral Samples .....   | 29   |
| 2.3.4 Total Dissolved Iron and Soluble Reactive Phosphate from Mineral Sorption<br>Experiments .....                           | 33   |
| 2.3.5 XAS Redox Experiments with MBS .....   | 36   |
| 2.3.6 XAS Time Series Experiments with Mineral Spiked MBS .....  | 45   |
| 2.4 Discussion .....   | 48   |
| 2.4.1 Missisquoi Bay Sediment Redox Properties and Fe/P Cycling .....  | 48   |
| 2.4.2 Iron Mineral Redox Properties and Fe/P Cycling .....   | 54   |
| Chapter Three: Conclusions and Future Directions .....   | 60   |
| 3.1 Conclusions and Reflection from Existing Research .....  | 60   |
| 3.2 Future Needs .....   | 61   |
| References .....   | 62   |
| Curriculum Vitae   |      |

## LIST OF TABLES

|   |    |
|---|----|
| Table 1: Initial Mineral Forms of Fe in Sediment and Time Scales of Reductive<br>Dissolution [1]. .....   | 9  |
| Table 2: Significance of Selected Energies for Phosphorus Multi-Energy Mapping. ....  | 23 |
| Table 3: Rate Constants ( $k$ ) and Linear Fit $R^2$ Values for Reduction Rates of<br>Pure 2-Line Ferrihydrite and Goethite Minerals Samples with Sorbed<br>Phosphate. .... | 32 |
| Table 4: Linear Combination Fitting Results Fitted to Ferrihydrite and Goethite<br>Standards from XANES Spectra Taken for the Oxidized Sample of MBS.....                   | 51 |
| Table 5: Linear Combination Fitting Results Fitted to Ferrihydrite and Goethite<br>Standards from XANES Spectra Taken for the Untreated Sample of MBS.....                  | 52 |

## LIST OF FIGURES

|   |    |
|---|----|
| Figure 1: Model for precipitate formation during Fe (II) oxidation with increasing initial P/Fe ratios where Fe(II) <sub>aq</sub> is aqueous Fe(II), Fe-Phos is Fe(III) phosphate with a P/Fe ratio of 0.55, HFO-P is hydrous ferric oxide with a P/Fe ratio of 0.25, and Lp* is lepidocrocite, goethite, and other poorly crystalline minerals related to lepidocrocite [2].                     | 18 |
| Figure 2: Dynamic of change in iron oxide mineralogy during mediated chronoamperometric reduction experiments of ferrihydrite to goethite and magnetite [3].  | 22 |
| Figure 3: Model of electron transfer pathways for non-mediated and mediated electrochemical analyses [4].   | 23 |
| Figure 4: Schematic diagram modeling steps followed to obtain the sorbed sample and reduced sample for SRP and TDFe analyses in sorption experiments.   | 30 |
| Figure 5: Chronoamperometric curves for reduction (positive current axis) and oxidation (negative current axis) for varying masses of MBS in 3 mL of PIPES buffer solution. Each curve represents the baseline subtracted reduction and oxidation curves for MBS samples.   | 33 |
| Figure 6: EEC of MER (blue) and MEO (red) experiments conducted on varying masses of MBS with 20% standard deviation.   | 34 |
| Figure 7: Plot of released SRP (A) and TDFe (B) as a function of reacted MBS sample mass with no added phosphate. Red data points represent samples analyzed after MEO and blue data points represent samples analyzed after MER.   | 36 |
| Figure 8: Plot of released SRP (A) and TDFe (B) from 100 mg MBS samples as a function of added phosphate that was sorbed for 24 hours in a mixed solution (Figure 3). Grey data points represent the “after sorption” sample while blue data points represent the “after reduction” reduced using MER. Standard error is represented as the standard deviation from three trials for each sample. | 37 |
| Figure 9: Mineral reduction extents from MER curves for 5 mg ferrihydrite (red) and goethite (yellow) samples with 20% standard deviation.  | 38 |
| Figure 10: First order rate constant plots for (A) ferrihydrite samples and (B) goethite samples with sorbed phosphate with starting concentrations from 0-400 ppm phosphate.   | 40 |
| Figure 11: SRP and TDFe as a function of sorbed phosphate after sorption (A) and after reduction (B) with 5 mg samples of pure 2-line ferrihydrite. Errors bars were calculated using the standard deviation of three absorbance spectroscopy samples for each MER trial.   | 43 |
| Figure 12: SRP and TDFe as a function of sorbed phosphate after sorption (A) and after reduction (B) with 5 mg samples of pure goethite. Errors bars were calculated using the standard deviation of three absorbance spectroscopy samples for each MER trial.  | 44 |
| Figure 13: $\mu$ -XRF map of an oxidized sample of MBS sediment near the Fe k-edge energy, 7150 eV, and XANES data corresponding to sediment grains indicated by the plot markers. The scale bar represents 200 microns.  | 47 |

|   |    |
|---|----|
| Figure 14: Title of Figure $\mu$ -XRF map of an untreated sample of MBS sediment near the Fe k-edge energy, 7150 eV, and XANES data corresponding to sediment grains indicated by the plot markers..... | 48 |
| Figure 15: $\mu$ -XRF map of a reduced sample of MBS sediment near the Fe k-edge energy, 7150 eV, and XANES data corresponding to sediment grains indicated by the plot markers.....                    | 49 |
| Figure 16: $\mu$ -XRF map of an oxidized sample of MBS sediment near the P k-edge energy, 2160 eV, and XANES data corresponding to sediment grains indicated by the plot markers.....                   | 50 |
| Figure 17: $\mu$ -XRF map of an untreated sample of MBS sediment near the P k-edge energy, 2160 eV, and XANES data corresponding to sediment grains indicated by the plot markers.....                  | 51 |
| Figure 18: $\mu$ -XRF map of a reduced sample of MBS sediment near the P k-edge energy, 2160 eV, and XANES data corresponding to sediment grains indicated by the plot markers.....                     | 52 |
| Figure 19: Time series $\mu$ -XRF maps from a sample of MBS with 25% ferrihydrite added after times 0, 15, 30, 60, and 300 minutes with corresponding XANES spectra.....                                | 54 |
| Figure 20: Time series $\mu$ -XRF maps from a sample of MBS with 25% goethite added after times 0, 15, 30, 60, 240, and 300 minutes with corresponding XANES spectra.....                               | 55 |

## LIST OF ABBREVIATIONS

|                               |   |
|-------------------------------|---|
| ABTS                          | 2,2'-azino-di-(3-ethylbenzthiazoline sulfonic acid) |
| Ag/AgCl                       | silver/silver chloride                              |
| C                             | carbon  |
| DO                            | dissolved oxygen                                    |
| DOP                           | dissolved organic phosphorus                        |
| DQ                            | diquat dibromide                                    |
| EAC                           | electron accepting capacity                         |
| EDC                           | electron donating capacity                          |
| EEC                           | electron exchange capacity                          |
| Fe                            | iron  |
| GCE                           | glassy carbon electrode                             |
| HABs                          | harmful algal blooms                                |
| MEO                           | mediated electrochemical oxidation                  |
| MER                           | mediated electrochemical reduction                  |
| MBS                           | Missisquoi Bay sediment                             |
| N                             | nitrogen  |
| P                             | phosphorus  |
| PCA                           | principle component analysis                        |
| PO <sub>4</sub> <sup>3-</sup> | phosphate   |
| Pt                            | platinum  |
| PIPES                         | piperazine-N,N'-bis(2-ethanesulfonic acid)          |
| SRP                           | soluble reactive phosphorus                         |
| SWI                           | sediment water interface                            |
| TDFe                          | total dissolved iron                                |
| XANES                         | x-ray absorption near-edge spectroscopy             |
| XAS                           | x-ray absorption spectroscopy                       |
| XRF                           | x-ray fluorescence                                  |
| μ-XRF                         | micro-x-ray fluorescence                            |

# CHAPTER ONE: A REVIEW OF RELEVANT LITERATURE AND OVERVIEW OF EXPERIMENTAL TECHNIQUES

## 1.1 Introduction

### *1.1.1 Motivation*

The goals of this research and thesis are to further understand redox cycling of iron and phosphorus in the context of mechanisms that drive Fe and P mobility between sediment and water, and the fate of these chemicals as a result of such reactions. There is agreement on the overall factors that influence redox behavior of sediments in eutrophic lake systems, however specific mechanisms that occur on smaller scales specific to the sediment water interface rely on processes that are less understood in comparison to overall conditions of lake systems. Mediated electrochemical experiments are a way to manipulate redox reactions in solutions with both aqueous and solid slurries of chemical interest. We aim to utilize these methods to control electron transfer in naturally heterogeneous samples and characterize redox and geochemical properties of both solutions and solids present as a result of controlled reduction and oxidation extents.

### *1.1.2 Hypothesis and Research Questions*

We tested several hypotheses with the planned experiments and data analysis associated with our analytical methods involving mediated electrochemical redox, spectrophotometry, and x-ray absorption spectroscopy experiments. We hypothesize that mediated electrochemical oxidation (MEO) and reduction (MER) techniques can be utilized to drive bulk material transformation mechanisms that can control P mobility and subsequent geochemical analyses can characterize redox properties and mineral compositions of natural and synthesized sediment samples. If redox driven oxidation of sediments occurs, phosphate release from the solid phase in sediments to the aqueous phase will mimic reactions in lacustrine systems where phosphate is released from sediments and becomes bioavailable due to dephosphorylation reactions. If redox driven reduction of sediments with Fe oxide minerals occurs, phosphate release from the solid phase in sediments will mimic reactions that take place during periods of hypoxia, and

bioavailability of phosphate in the water column may be inhibited due to precipitation of ferrous Fe-P minerals, such as vivianite. To test our hypotheses, we planned experiments to evaluate the following research statements.

1. Mediated electrochemical experiments can be used to drive reactions of naturally-occurring, heterogenous sediment samples.
2. Phosphate concentrations and interactions with influence the redox properties of iron (oxyhydr)oxide minerals and cycling mechanisms between sediment and water.
3. Analytical techniques can be used to characterize solution chemistry after mediated electrochemical redox reactions, and these species can indicate that phosphate and iron are released from sediments as a result of oxidation, reduction, or both.
4. Spatial and chemical characteristics of sediments subjected to mediated electrochemical experiments can be described with  $\mu$ -XRF mapping and XANES analyses.
5. Chemical characteristics may indicate that reprecipitation of ferrous Fe-P minerals, like vivianite, occur as a result of reduction, and we can determine the saturation threshold for precipitation of these minerals to reduce bioavailable phosphate.

## 1.2 Literature Review

### *1.2.1 Phosphorus in Our Environment: Nutrient and Contaminant*

Phosphorus (P) is a ubiquitously distributed and naturally occurring critical nutrient that plays many essential functions in the corners of biology, chemistry, and geology. It is the 11<sup>th</sup> most abundant element in the lithosphere [5], on average making up about 0.09 weight percent of the Earth's crust [6]. P in the environment typically exists as the oxyanion phosphate ( $\text{PO}_4^{3-}$ , or orthophosphate) [5] originating from mechanical and chemical weathering of sedimentary and igneous minerals, namely variations of apatite [6]. Organic phosphorus ( $\text{P}_{\text{org}}$ ) is a complex mix of molecules resulting from biological activity, as phosphorylation pathways of  $\text{P}_{\text{org}}$  formation are a high-energy processes that

does not occur abiotically in bulk solution [7, 8], but rather is a critical component of life processes that are ubiquitous in biochemistry [9]. Natural sources of P were more significant in the P cycle historically as human activities have evolved to dominate the modern cycle through mining of rock phosphate, transport and application of concentrated phosphorous as fertilizer for global food production, sewage and waste sources, deforestation, and watershed transport of excess phosphorus from watersheds to basins, and will likely impact it for hundreds of years to come [6]. There are no environmentally significant gaseous phases [6], so we focus on transitions between solid and aqueous phases. P released from natural and anthropogenic sources is transported into various environmental reservoirs and sinks including soils, sediments, and water bodies – both terrestrial and marine. In aquatic environments, P is commonly partitioned into particulate and dissolved P, the latter of which includes soluble reactive P (SRP, largely as orthophosphate) and dissolved organic P (DOP) [10]. Cycling of these forms of P, between particulate in sediments and dissolved in water rely heavily on conditions influencing the sediment water interface (SWI), including mineral dissolution and precipitation, mineral sorption and desorption, and biochemical phosphorylation and dephosphorylation [11-13]. There are many aspects of P transport and cycling that are well researched, yet there are still many questions regarding specific mechanisms of loading, cycling, and bioavailability of P in aquatic systems. With heavy reliance on P for function in our environment especially for global food production [5], it is important that we continue to expand our knowledge of the mechanisms by which P is transported and recycled in modern and ancient environments.

P is an essential element for all forms of life, and limits biological productivity in many terrestrial and marine environments [5, 14]. While P is essential for biological function and growth, excessive amounts may lead to harmful effects through eutrophication. Eutrophication is defined as a process by which nutrient content in aquatic environments is increased, characterized by excessive plant and algal growth from limiting factors contributing to photosynthesis [15, 16], specifically nitrogen (N) and P. Eutrophication is a critical problem in surface water quality in the U.S. [17]. Promotion of biological growth from eutrophic environments results in a cascade of impactful events. Cyanobacterial growth in nutrient-rich environments causes harmful

algal blooms (HABs) that limit water clarity, deplete oxygen, and may form toxic secondary metabolites [18]. This can lead to further water quality impairment including but not limited to fish kills, unpalatability and toxicity of drinking water, and reduction of recreational activities [17]. Eutrophication occurs in both freshwater and marine environments. Many freshwater lakes exhibit recurring eutrophication and HABs, including Lake Champlain which has experienced increasingly severe HABs in recent history [19]. Not only can we witness severe re-eutrophication due to increased nutrient loading and eutrophication in Lake Champlain, but also other waterbodies around the world including an abundance of shallow lakes distributed around China [20], Lake Valencia in Venezuela [21], Lake Victoria in Africa [22], and Lake Erie in the United States [23].

Impacts of HABs have increased over the past several decades due to continuous loading from anthropogenic sources and climate change [18]. Demands for P in various industries worldwide have led to increased anthropogenic production and use of P-containing materials, especially phosphate-rich fertilizers to maintain crop production sufficient to sustain adequate food growth with an exponentially growing population. The agriculture industry has become the number one user of global P accounting for 80-90% of the world's total demand [24]. Large quantities of P are used on farmlands, typically with large preexisting P reserves, and in many areas inputs from fertilizers outweigh outputs from produce [15]. P imbalance, combined with long-term land applications and water runoff, cause agricultural land to serve as a major non-point source for P pollution in bodies of water, often aggravated by the proximity of agricultural environments to P-sensitive water bodies, especially lakes [17]. Phosphate compounds in natural water have relatively low solubility and concentrations of 0.08 to 0.10 mg/L may trigger periodic blooms; however, long-term eutrophication is usually prevented if total P and  $\text{PO}_4^{3-}$  levels are below 0.5 mg/L and 0.05 mg/L respectively [5]. Continuous P loading from non-point source pollution inhibits eutrophic environments from recovering as they bioaccumulate P within the system over time [13].

### *1.2.2 Internal Loading of P in Terrestrial Aquatic Systems*

The risk of eutrophication in terrestrial aquatic systems makes estimating and understanding P cycling in these environments a critical step in evaluating water quality and implementing remediation techniques. While P runoff from agricultural land is a major component of non-point source P pollution [17], other non-point sources such as wastewater and sewage effluent have contributed to continuous loading of P in ecologically sensitive areas [25]. Concerns have also been raised about potential P entering water bodies from P-rich sediment, also known as “internal loading”. Non-point source contamination of P in lakes and sedimentation over time has created “legacy P” that resides within the sediments of lake environments. Internal loading of P in lakes comes from mobilization of P to water from within the environment, such as release of P sorbed to minerals in sediments. Scientists predict that internal loading of P from legacy P in sediments may be a critical issue preventing eutrophic environments from recovering [13]. Studies have aimed to estimate P budgeting and cycles in aquatic environments; however, internal loading of P from sediments to surface water remains poorly understood and results in the largest likely source of error for P cycling models [13].

It has been widely demonstrated that sediments serve as redox-mediated P-buffers, where P is retained in the solid phase under oxic conditions and released into the aqueous phase under anoxic conditions [26]. Seasonal changes in physical and chemical properties drive changes in P chemistry and P mobility between sediment and water, the primary mechanism of internal loading. Benthic cycling of P in sediments depends highly on redox regimes within superficial sediments. These cycling mechanisms are especially dynamic in shallow waters [13]. Shallow waters are more susceptible to environmental damage from sediment P internal loading due to closer proximity to the photic zone, less volume for dilution of P loading [27], and more dynamic changes in temperature and O<sub>2</sub> exchange between water and the atmosphere driven by hydrodynamics. While P itself is not typically redox-active in the environment, its cycle is closely coupled to that of other redox-sensitive elements such as iron (Fe) and carbon (C) [13]. Fe has been shown to be a major driver in cycling of P between sediment and water [28]. Phosphate exhibits a high affinity for Fe and has a closely coupled cycling mechanism strongly influenced by redox-transformations between relatively soluble ferrous Fe(II) and poorly soluble ferric

Fe(III) [2], that are driven by both biotic and abiotic redox mechanisms. The seasonal redox cycling of Fe resulting in P cycling between sediment and water has been referred to as Fe pumping [12].

### *1.2.3 Oxidizing Conditions*

Under oxidizing conditions Fe(II) loses electrons to form less soluble Fe(III), resulting in precipitation of Fe (oxyhydr)oxide (hereon referred to as iron oxides for simplicity) minerals including but not limited to ferrihydrite, goethite, hematite, and magnetite through a series of mechanisms including deprotonation, hydrolysis, crystallization, and dehydration reactions [17]. Formation of the more poorly soluble Fe minerals is primarily dependent on how these different mechanisms drive recrystallization over time, following Ostwald ripening where smaller and less stable particles form initially, followed by recrystallization and transformation to more thermodynamically stable minerals and larger size particles. Oxidation of aqueous Fe(II) leads to initial formation of amorphous to poorly crystalline nanoscale Fe(III) precipitates like (2-line, 6-line)ferrihydrite [15] that are formed via pathways of deprotonation followed by crystallization of mineral grains. These initial precipitates are often characterized as hydrous ferric oxides (HFO) but are most often actually nanoparticulate minerals. After formation of these poorly crystalline forms, further oxidation-driven precipitation and ripening drives transformation of ferrihydrite minerals to more stable minerals, like goethite [18], via hydrolysis mechanisms. More stable forms like hematite and magnetite have longer precipitation timescales and ripen into larger crystals with lower surface area than less stable minerals. Due to more rapid precipitation, poorer crystallinity, less thermodynamic stability, smaller particle sizes and higher surface area, Fe(III) mineral precipitates ferrihydrite and goethite are more dynamic in Fe pumping.

Fe oxides have hydroxyl substituents (-OH) that serve as sorption sites for phosphate on the mineral surface. Phosphate may form inner sphere complexes between the phosphate oxygens and hydroxyl oxygens or outer sphere complexes arising from electrostatic interactions of phosphate and iron-hydroxide (Fe-OH<sub>2</sub>) groups [29]. Of all the metal oxide particles, amorphous Fe oxides have the greatest adsorption capacity for

phosphate [30], primarily due to their high surface area and low thermodynamic stability. This means that forms like ferrihydrite and goethite are critical in understanding P-coupled cycling mechanisms driven by redox changes. Phosphate sorption onto Fe oxides results in retainment of phosphate in the solid phase. As Fe(II) oxidizes with increasing dissolved phosphate concentrations, formation of Fe oxides decreases and formation of Fe (III) phosphates can be expected as shown in Figure 1 [2]. At lower P:Fe ratios, oxidation drives formation of P-sorbed Fe oxide minerals, and at P:Fe ratios above 0.55 formation of primarily Fe-phosphate minerals is expected due to geochemical saturation. It has been shown that oxidation reactions likely play a large role in Fe/P species present in sediments [12] that are readily available for reductive dissolution when conditions may change.

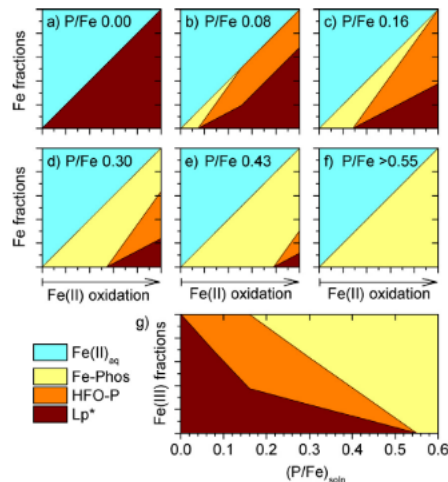


**Figure 1.** Model for Precipitate Formation During Fe (II) Oxidation with Increasing Initial P/Fe Ratios, Where  $\text{Fe(II)}_{\text{aq}}$  is Aqueous Fe(II), Fe-Phos is Fe(III) Phosphate with a P/Fe Ratio of 0.55, HFO-P is Hydrrous Ferric Oxide with a P/Fe Ratio of 0.25, and  $\text{Lp}^*$  is Lepidocrocite, Goethite, and Other Poorly Crystalline Minerals Related to Lepidocrocite [2].

#### 1.2.4 Reducing Conditions

Oxidized forms of Fe minerals present in sediments or suspended in solution are potentially available for changes driven by subsequent reducing conditions in redox-dynamic settings [13, 31]. Under reducing conditions, solid Fe (III) minerals gain electrons forming Fe(II), which is relatively soluble at neutral pH in comparison of

Fe(III). The release of Fe(II) into solution as a result of reduction is referred to as reductive dissolution of Fe. Table 1 shows varying time scales for reductive dissolution of Fe(III) minerals based on thermodynamic stability. Poorly crystalline Fe(III) minerals like ferrihydrite and lepidocrocite dissolve on shorter time scales of hours to days. As thermodynamic stability increases, Fe minerals will take longer to dissolve. While goethite and hematite categorized together in Table 1, goethite is less stable and reductively dissolves more quickly. The reductive dissolution sequence behaves in contrast to the precipitation and ripening sequence making goethite the next mineral to dissolve after ferrihydrite. Fe oxides like hematite and magnetite require longer time scales for reductive dissolution. These more stable minerals are less critical in understanding the coupled redox cycling of Fe and P on the seasonal scale, as seasonal cycling occurs on shorter time scales and these minerals exhibit a much lower affinity for phosphate sorption. Reductive dissolution of Fe(III) minerals not only results in release of Fe(II) but also release of phosphate sorbed to the minerals. Faster reductive dissolution of poorly crystalline Fe(III) minerals in addition to their greater sorption capacity for P support that these phases are critical for P mobility linked to Fe pumping. Release of Fe(II) and phosphate from sediments may result in internal loading in lakes but mechanisms of release and fate of the ions are not well understood in all systems. From studies with Lake Pavin, France, reductive dissolution of Fe oxide minerals with sorbed P results in vivianite formation ( $\text{Fe}_3(\text{PO}_4)_2$ ) [12], however some phosphate may be made bioavailable for other fates involving eutrophication and HABs. A fundamental question arises how thermodynamic and kinetic limitations of sorption of P to Fe(III) minerals and precipitation of Fe(II)-P minerals like vivianite control P mobility linked to Fe pumping.

**Table 1** Time scales for reductive dissolution of different sedimentary iron minerals\*

| Iron mineral phase  | Time scale for reductive dissolution  | Operational phase in which these iron mineral phases are extracted ** |
|---|---------------------------------------|---|
| amorphous, poorly crystalline iron oxides (e.g., lepidochrochite or ferrihydrite) | hours to days                         | Fe <sub>ox</sub>  |
| more crystalline iron oxides (e.g., goethite or hematite)                         | days to months                        | Fe <sub>ox</sub>  |
| magnetite   | months to ~10 <sup>2</sup> yr         | Fe <sub>mag</sub>   |
| “structural” iron in sheet silicates  | ~10 <sup>2</sup> – 10 <sup>5</sup> yr | Fe <sub>prs</sub>   |
| “refractory” iron minerals (e.g., ilmenite or amphiboles)                         | > ~10 <sup>5</sup> yr                 | Fe <sub>U</sub>   |

\* modified from results presented in Canfield et al. (1992), Raiswell and Canfield (2012) and Poulton and Raiswell (2002).

\*\* see section III.B.2 for details

**Table 1.** Initial Mineral Forms of Fe in Sediment and Time Scales of Reductive Dissolution [1].

### 1.2.5 Coupled Redox Cycling and Algal Blooms

The coupled redox mechanisms of Fe drive coupled changes in P cycling between sediment and water and effect P mobility through both time and space. Biogeochemical cycling of Fe and P is driven both by temporal and hydrodynamic variations that effect SWI geochemistry of systems over time periods ranging from hours to months [31-33]. Observed changes in SWI geochemistry are closely correlated to algal blooms and cyanobacterial presence, specifically in shallow waters [32, 34]. During the winter season, ice-cover plays an important role in isolating internal lake processes resulting in internal loading and Fe pumping due to suboxic conditions near the SWI. With suboxic conditions under ice cover, reductive dissolution of Fe and concurrent release of P from sediments increases the concentration of these materials in the water column [33]. Reductive dissolution during ice cover is driven by O<sub>2</sub> consumption, limited O<sub>2</sub> introduction from air due to ice barriers, and reduced circulation of water [35]. As thermal stratification stabilizes the water column and phosphate flux from sediments increases aqueous availability of P, warmer months bring algae and cyanobacterial blooms as they consume P in the water column. As blooms persist, sediment P continues to decrease as waters remain relatively stratified and DO penetration with depth is low [32]. As blooms end and wind and thermal mixing shift the hydrodynamic stability of

shallow systems, biogeochemical shifts cause reprecipitation of minerals and Fe and P flux back into sediments [19]. The sediment cycle then continues into cold seasons where lakes are restabilized and flux of Fe and P from sediments increases again. The seasonal cycling of Fe and P near the SWI offers a broad perspective, however hourly and daily changes also occur [31]. As we know that less stable Fe(III) minerals precipitate and dissolve over relevant brief time scales, these are the focus of our research in understanding Fe and P cycling between sediments and water.

#### *1.2.6 Mediated Electrochemical Approaches to Control Redox Reactions*

The objective driving this research is to explore the sequence of Fe and P mineral paragenesis over time while driving reduction reactions of ferrihydrite and goethite with sorbed P and determine thermodynamic limits of resulting mineral precipitation and ion release into solution. Our approach to experiment with P and Fe dynamics during redox reactions will use techniques similar to those explored and characterized by Meret Aeppli et. al. [3, 36]. This previous research uses mediated electrochemical reduction (MER) techniques to explore rates and extents of iron (oxyhydr-)oxide reduction and quantify reduction of ferrihydrite, goethite, and hematite over a range of negative reaction free energies and during transformation of ferrihydrite into more crystallized Fe oxides [3, 36]. MER is a powerful technique that can be used to control redox potential over time and quantify the rate and extent of reactions for a species of interest. The measurements are recorded as a function of current which can be used to calculate the amount of electrons transferred in bulk solution as a function of time. MER, rather than non-mediated electrochemical reduction, provides faster reaction times for reduction as well as eliminates matrix effects caused by pH changes by using a non-proton coupled mediator molecule [3]. Reaction free energies vary by modifying solution pH and reduction potentials for reactions of the various iron oxides, and it is apparent that different Fe oxide minerals exhibit different reduction capabilities with varying free energy. In the experiments by Aeppli et al mentioned above, ferrihydrite reduction was fast at all tested free energies due to its low thermodynamic stability, while goethite and hematite reduction were more incomplete and slow with increasingly less reaction driving force [36]. Conclusions of previous MER research support evidence of reactions

driven by thermodynamic stability of the iron oxide minerals, where ferrihydrite, goethite, and hematite had more increasingly slow and incomplete reduction respectively [36]. Extents of reactions, and electron accepting capacities of these synthesized minerals, are calculated using equation 1,

$$q(t_{\text{end}}) = \frac{1}{F} \int_{t_0}^{t_{\text{end}}} I(t) dt$$

**Equation 1.** Integrated area under a chronoamperometric curve to calculate electron exchange capacities for reduction or oxidation.

where  $F$  is Faraday's constant and  $I$  is current measured over time [36]. This technique was progressed by further examining ferrous iron-induced electron transfer to 6-line ferrihydrite by subjecting suspensions of ferrihydrite to varying concentrations of  $\text{Fe(II)}$  solution, Formation of more crystalline minerals occurred over time in the presence of aqueous  $\text{Fe(II)}$  [3]. As Ostwald ripening occurred with pre-existing ferrihydrite and  $\text{Fe(II)}$  in solution, more stable minerals goethite and magnetite eventually precipitated at longer time scales. At neutral pH,  $\text{Fe(II)}$  induced transformation of ferrihydrite resulted in initial formation of mostly goethite, however a small amount of magnetite was formed as time increased. These transformation experiments resulted in reducibility of the created minerals in agreement with initial study results[36]: ferrihydrite was complete and fast at all tested pH values while goethite and magnetite rate and extent of reduction decreased with increasing pH, and therefore decreasing reaction free energy. Decreases in Fe-oxide reducibility can be linked to concurrent changes in the iron mineralogy and thermodynamic stability, shown in figure 2 [3]. These results further emphasize the importance of less thermodynamically stable Fe oxides in P cycling, as they are more readily transferred between the solid and aqueous phases in lower energy systems.

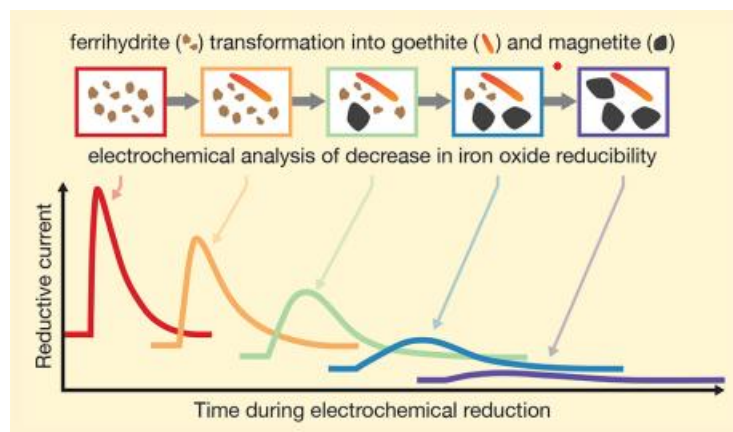


**Figure 2.** Dynamic of Change in Iron Oxide Mineralogy During Mediated Chronoamperometric Reduction Experiments of Ferrihydrite to Goethite and Magnetite [3].

### 1.3 Experimental Overview

#### 1.3.1 Mediated Electrochemical Techniques

MER is a powerful tool that has been widely used to control electron transfer to and from electroactive species in solution. Several studies have explored this technique specifically with focus on redox-active iron minerals [3, 4, 36]. A major goal of this research is to expand the use of MER techniques to explore reactions of Fe-oxides and natural sediment samples with sorbed phosphate, to mimic reactions occurring in lacustrine systems. MER utilizes an electroanalytical method called chronoamperometry, where a known potential, measured in volts (V), is applied to a system and the current, in amps or microamps (A/ $\mu$ A), is measured over time [37]. The current response in chronoamperometric experiments represents the faradaic current driven by direct redox changes of the species of interest; however, conventional non-mediated approaches can exhibit sluggish kinetics of electron transfer between the working electrode and species of interest [4]. Mediated chronoamperometric techniques utilize a dissolved electron transfer mediator to facilitate electron transfer from the working electrode and the geochemical phase added to the cell [36]. Figure 3 presents a graphic model comparing mediated versus non-mediated techniques [4]. The single-electron transfer mediator assists in overcoming slow reactions and provides a non-proton-coupled reactions to avoid

changes in system pH, which would otherwise affect redox reaction rates and extents [3, 36]. The technique requires collection of two time-integrated current curves: one initially for the redox reaction of the selected mediator and one subsequently for the redox reaction resulting from the geochemical phase. From the latter curve, we can determine the reaction extents (for known concentrations) and rates. MER is highly sensitive and ideal for work with low concentrations, and it can be used to explore redox properties of minerals and sediments in solution.

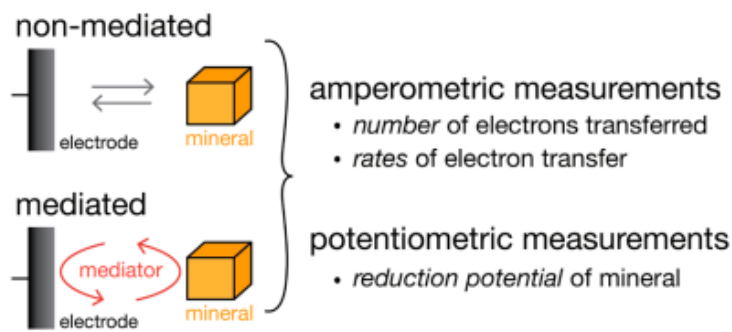


**Figure 3.** Model of Electron Transfer Pathways for Non-Mediated and Mediated Electrochemical Analyses [4].

### 1.3.2 $\mu$ -X-Ray Fluorescence (Multi-)Energy Mapping

Mediated electrochemical redox techniques are used to quantify electron transfer properties but must be coupled with additional analytical techniques to determine concurrent changes in geochemical composition. Micro X-ray fluorescence ( $\mu$ -XRF) energy mapping offers high-resolution elemental mapping images using position tagged spectroscopy (PTS) [38]. At any selected energy or multiple energies, elemental maps are created across a specified sample using raster imaging and PTS to capture relative counts of energy for each pixel. These maps are helpful for determining abundance and spatial distribution of elements in a sample. The specified energy at which the map is taken can be selected to target a specific element, compound, or mineral. As different geochemical phases of elements have unique energy spectra (more in next section), maps with differing energies can target different minerals. In this research, we use  $\mu$ -XRF mapping to determine Fe and P mineral distribution in mounted sediment samples throughout MER or MEO changes. Initially maps are obtained at the k-edge energy required for core electron excitation from the 1s orbital of Fe and the P in phosphate. After acquiring

‘total’ P, multi-energy maps are taken to characterize spatial abundance and distribution of different phosphate minerals that may exhibit differences in redox activity.

### *1.3.3 X-Ray Absorption Near Edge Structure Spectroscopy*

X-ray absorption near edge structure (XANES) spectroscopy analysis is critical to determining what geochemical form of mapped elements reside in a sample. In XANES, a photon is absorbed, and with enough energy an electron is excited from a core state to an empty state [39]. This excitation emits resulting energy that is recorded as a function of energy, in electron volts (eV), applied to the system. Since each element has a unique core-level energy, XANES is a selective technique that can be used to identify minerals of specific elements based on elemental electron excitation energies. An energy beam of specified diameter targets a sample spot, and the beam energy is scanned, enveloping the k-edge energy required to excite an electron from the element, and electron orbital of that element, of choice. This results in a k-edge energy peak for the element. Different spectral features surrounding the k-edge peak, known as pre-edge and post-edge features, are used to delineate specific bonding changes associated with complexation and mineralization. Energies can also be selected for different outer orbital electron excitations, XANES allows for identification of elemental oxidation states [40, 41], mineral forms [41, 42], and mineral changes in systems with space [12] and time [43]. In our case, XANES analyzes spots selected from  $\mu$ -XRF maps in attempt to characterize geochemical species of Fe and P within mounted sediment samples throughout redox changes.

## CHAPTER TWO: MEDIATED ELECTROCHEMICAL REDUCTION AS A TOOL TO CHARACTERIZE P AND FE CYCLING BETWEEN SEDIMENT AND WATER

### 2.1 Introduction

Phosphorus (P) plays a pivotal role in ubiquitous cycling mechanisms in the corners of biology, chemistry, and geology. P is the limiting nutrient in controlling biological productivity in both terrestrial and marine environments [5] and influences geochemical processes as it has closely coupled cycling mechanisms with other elements [13, 26, 44]. The modern day P cycle, contrary to the historical, is dominated by anthropogenic influencers and will continue to be for hundreds of years to come [6]. The agricultural industry is the largest user of P globally, accounting for 80-90% of the world's total demand [24], and this has led to increased use of P across terrestrial landscapes. Large quantities of P, namely in the form of phosphate or orthophosphate ( $\text{PO}_4^{3-}$ ) are used on farmlands, typically with large preexisting P reserves, and in many areas inputs from fertilizers outweigh outputs from produce creating excess P available for transport via surface runoff [15]. Along with application of concentrated phosphorous as fertilizer, mining of rock phosphate, sewage and waste sources, and deforestation contribute to excess P available for transport from watersheds to basins. P imbalance, combined with long-term land applications and water runoff, cause agricultural land to serve as a major non-point source for P pollution in bodies of water, often aggravated by the proximity of agricultural environments to P-sensitive water bodies, especially lakes [17].

While essential for biological function, excess P introduction to aquatic environments, both terrestrial and marine, may lead to harmful effect through eutrophication; a process by which nutrient content in aquatic environments is increased, characterized by excessive plant and algal growth from limiting factors contributing to photosynthesis [15, 16] and a critical problem in surface water quality in the U.S. [17]. Cyanobacterial growth in eutrophic environments cause harmful algal blooms (HABs) that limit water clarity, deplete oxygen, and form toxic secondary metabolites [18] resulting in further damage to fish populations, water palatability, and recreational activities [17]. Many freshwater lakes exhibit recurring eutrophication and HABs,

including Lake Champlain in the United States which has experienced increasingly severe HABs in recent history [19], an abundance of shallow lakes distributed around China [20], Lake Valencia in Venezuela [21], Lake Victoria in Africa [22], and Lake Erie in the United States [23], to name a few. The risk of eutrophication in terrestrial aquatic systems makes estimating and understanding P cycling in these environments a critical step in evaluating water quality and implementing remediation techniques. While P runoff from agricultural land is a major component of non-point source P pollution [17], other non-point sources such as wastewater and sewage effluent have contributed to continuous loading of P in ecologically sensitive areas [25]. Concerns have also been raised about potential P entering water bodies from P-rich sediment, through a process known as “internal loading”. Non-point source contamination of P in lakes and sedimentation over time has created “legacy P” that resides within the sediments of lake environments. Internal loading of P in lakes comes from mobilization of P to water from within the environment through release of P sorbed to minerals in sediments. Scientists predict that internal loading from legacy P in sediments may be a critical issue preventing eutrophic environments from recovering [13]. Studies have aimed to estimate P budgeting and cycles in aquatic environments; however, internal loading of P from sediments to surface water remains poorly understood and results in the largest likely source of error for P cycling models [13].

It has been widely demonstrated that sediments serve as redox-mediated P-buffers, where P is retained in the solid phase under oxic conditions and released into the aqueous phase under anoxic conditions [26]. Seasonal changes in physical and chemical properties drive changes in P chemistry and P mobility between sediment and water, the primary mechanism of internal loading. Benthic cycling of P in sediments depends highly on redox regimes within superficial sediments. These cycling mechanisms are especially dynamic in shallow waters [13]. Shallow waters are more susceptible to environmental damage from sediment P internal loading due to closer proximity to the photic zone, less volume for dilution of P loading [27], and more dynamic changes in temperature and O<sub>2</sub> exchange between water and the atmosphere driven by hydrodynamics. While P itself is not typically redox-active in the environment, its cycle is closely coupled to that of other redox-sensitive elements such as iron (Fe) and carbon (C) [13]. Fe has been shown to be

a major driver in cycling of P between sediment and water [28]. Phosphate exhibits a high affinity for Fe and has a closely coupled cycling mechanism strongly influenced by redox-transformations between relatively soluble ferrous Fe(II) and poorly soluble ferric Fe(III) [2], that are driven by both biotic and abiotic redox mechanisms. The seasonal redox cycling of Fe resulting in P cycling between sediment and water has been referred to as Fe pumping [12].

Under oxidizing conditions near the SWI, Fe(III) (oxyhydr)oxide (hereon referred to as iron oxides for simplicity) minerals precipitate forming ferrihydrite, goethite, hematite, and magnetite through a series of mechanisms including deprotonation, hydrolysis, crystallization, and dehydration reactions [17]. As these minerals precipitate, nanoparticulate materials form first followed by recrystallization and transformation to more thermodynamically stable minerals with larger particle sizes. Oxidation of aqueous Fe(II) leads to initial formation of amorphous to poorly crystalline nanoscale Fe(III) precipitates like (2-line, 6-line)ferrihydrite [15] that are formed via pathways of deprotonation followed by crystallization of mineral grains. These initial precipitates are often characterized as hydrous ferric oxides (HFO) but are most often actually nanoparticulate minerals. After formation of these nanoparticulate forms, further oxidation-driven precipitation and ripening drives transformation of ferrihydrite minerals to more stable minerals, like goethite [18], via hydrolysis mechanisms. More stable forms like hematite and magnetite have longer precipitation timescales and ripen into larger crystals with lower surface area than initially forming minerals. Fe oxides have hydroxyl substituents (-OH) that serve as sorption sites for phosphate on the mineral surface. Phosphate may form inner sphere complexes between the phosphate oxygens and hydroxyl oxygens or outer sphere complexes arising from electrostatic interactions of phosphate and iron-hydroxide (Fe-OH<sub>2</sub>) groups [29]. Of all the metal oxide particles, amorphous Fe oxides have the greatest adsorption capacity for phosphate [30], primarily due to their high surface area and low thermodynamic stability. Due to more rapid precipitation, poorer crystallinity, less thermodynamic stability, smaller particle sizes, and higher surface area, Fe(III) mineral precipitates ferrihydrite and goethite are more dynamic in Fe pumping and internal loading mechanisms. Phosphate sorption onto Fe oxides results in retainment of phosphate in the solid phase, reducing aqueous

bioavailable P. As Fe(II) oxidizes with increasing dissolved phosphate concentrations, formation of Fe oxides decreases and formation of Fe (III) phosphates can be expected [2]. It has been shown that oxidation reactions likely play a large role in Fe/P species present in sediments [12] that are readily available for reductive dissolution during subsequent periods of hypoxia.

Under reducing conditions, Fe oxide minerals release poorly soluble Fe(II) into solution, referred to as reductive dissolution. Similar to the formation pathways of Fe oxides, the more unstable HFO minerals are the first to reductively dissolve, followed by more stable forms like goethite [1]. As thermodynamic stability increases, Fe minerals take longer to dissolve. Poorly crystalline Fe(III) minerals like ferrihydrite dissolve on shorter time scales of hours to days, while goethite minerals dissolve on time scales ranging from days to months. Reductive dissolution of Fe(III) minerals not only results in release of Fe(II) but also release of phosphate sorbed to the minerals [13, 31]. Rapid reductive dissolution of poorly crystalline Fe(III) minerals in addition to their greater sorption capacity for P support the idea that these phases are critical for P internal loading linked to Fe pumping. Release of Fe(II) and phosphate from sediments may result in internal loading in lakes, but mechanisms of release and fate of the ions are not well understood in all systems. From studies in Lake Pavin, France, reductive dissolution of Fe oxide minerals with sorbed P in sediments results in vivianite formation ( $\text{Fe}_3(\text{PO}_4)_2$ ) [12], however some phosphate may be made bioavailable for other fates involving eutrophication and HABs. A fundamental question arises how thermodynamic and kinetic limitations of sorption of P to Fe(III) minerals and precipitation of Fe(II)-P minerals like vivianite control P mobility linked to Fe pumping.

The coupled redox mechanisms of Fe drive coupled changes in P cycling between sediment and water and affect P mobility through both time and space. Biogeochemical cycling of Fe and P is driven both by temporal and hydrodynamic variations that effect SWI geochemistry of systems over time periods ranging from hours to days to months [31-33]. Observed changes in SWI geochemistry are closely correlated to algal blooms and cyanobacterial presence, specifically in shallow waters [32, 34]. During the winter season, ice-cover plays an important role in isolating internal lake processes resulting in Fe pumping, and concurrent release of P from sediments increases the concentration of

these materials in the water column [33]. Reductive dissolution during ice cover is driven by O<sub>2</sub> consumption, limited O<sub>2</sub> introduction from air due to ice barriers, and reduced circulation of water [35]. As thermal stratification stabilizes the water column and phosphate flux from sediments increases aqueous availability of P, warmer months bring algae and cyanobacterial blooms as they consume P in the water column. As blooms persist, sediment P continues to decrease as waters remain relatively stratified and dissolved oxygen (DO) penetration with depth remains low [32]. As blooms end and wind and thermal mixing shift the hydrodynamic stability of shallow systems, biogeochemical shifts cause reprecipitation of minerals and Fe and P flux back into sediments during fall months [19]. The sediment cycle then continues into cold seasons where lakes are restabilized and flux of Fe and P from sediments increases again. The seasonal cycling of Fe and P near the SWI offers a broad perspective, however hourly and daily changes also occur [31]. As we know that less stable Fe(III) minerals precipitate and dissolve over brief time scales, these are the focus of our research in understanding Fe and P cycling between sediments and water. Understanding the specific cycling mechanisms of P with respect to Fe minerals may allow for better predictions and ultimately better conservation practices in prevention P loading and eutrophication in terrestrial aquatic systems. Mediated electrochemical techniques also offer an opportunity to control redox reactions within closed systems, and thus examine the redox controls on cycling mechanisms specific to Fe and P phases between sediment and water.

## 2.2 Methods

### *2.2.1 Mediated Electrochemical Reduction and Oxidation Experiments*

MER and MEO experiments were used to drive redox reactions of sediment slurries in a solution of pH 7 with a non-proton-coupled, single-electron transfer mediator. For both oxidation and reduction, the electrolytic cell contained a glassy carbon electrode (GCE) cup that served as a working electrode and solution vessel with a platinum (Pt) counter electrode versus a silver/silver chloride (Ag/AgCl) reference electrode. The cell was controlled by a wireless Bluetooth-enabled micro-potentiostat (DLK Micro-Pstat, Analytical Instrument Systems, Inc.) with continuous stirring to

observe measurements of bulk solution properties. MER experiments were performed in an anaerobic glovebox chamber (COY Laboratory Products, Inc.) using diquat dibromide (DQ) as the mediator species with reduction half-potential of  $E = -0.65$  V. Initial baseline current was reached by reacting 100  $\mu$ L of 10 mM DQ solution in 3 mL of piperazine-*N,N'*-bis(2-ethanesulfonic acid) (PIPES) buffer solution. When a stable background current was achieved, sediment slurries of either Missisquoi Bay sediment, synthesized ferrihydrite, or synthesized goethite were added to the cell and allowed to react until a new stable baseline current was obtained. MEO experiments were not kept in an anaerobic environment, and were ran using 100 mL of 10 mM solution of 2,2'-azino-di-(3-ethylbenzthiazoline sulfonic acid) (ABTS) as the mediator species with an oxidation half-potential of  $E = 0.55$  V. MER and MEO provide quantitative data about electron donating and accepting capacities (EAC and EDC), however other analytical techniques were coupled with these reactions to provide qualitative data about the states and cycling of P and Fe. The exact composition and concentrations of samples used vary based on the amount of phosphate added or omitted from experiments.

### 2.2.2 Phosphate Sorption Experiments

Sorption experiments were used to evaluate P and Fe concentrations in solution as soluble reactive phosphorus (SRP), also considered orthophosphate, and total dissolved iron (TDFe) after sorption of phosphate to sediment and sequential MER. For our natural MBS samples, we added 100 mg of sediment to a 5 mL centrifuge with 4 mL of starting known phosphate concentration ranging from 0-50 ppm. Solution slurries were mixed on a Labquake rotator overnight to allow equilibration of phosphate sorption, and two samples were taken from the equilibrated vial. For the “after sorption” sample, 1.5 mL was drawn into a syringe and pushed through a 0.2  $\mu$ m filter membrane. The filtered solution was kept frozen until further analysis. For the “after reduction” sample, 1 mL of solution was taken from the equilibration tube and put into the anaerobic glovebox. This sample was then reduced in our electrochemical cell, pushed through a 0.2  $\mu$ m filter membrane (Advantec) and the filtered solution was frozen until further analysis. For our pure mineral sorption experiments with ferrihydrite and goethite, 5 mg of each mineral sediment were added into the 4 mL solution of phosphate concentration ranging from 0-

400 ppm and the same procedure was followed to obtain the after sorption and after reduction samples. All liquid samples were then frozen for later analysis via absorbance spectrophotometry.

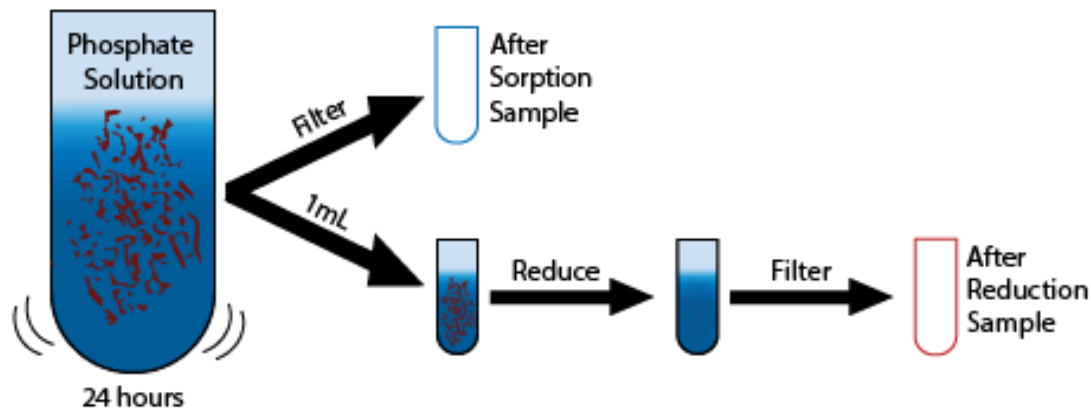


**Figure 4.** Schematic Diagram Modeling Steps Followed to Obtain the Sorbed Sample and Reduced Sample for SRP and TDFe Analyses in Sorption Experiments.

### 2.2.3 Spectrophotometry Techniques

SRP and TDFe for samples were analyzed using an Epoch 2 Microplate Reader (Biotek). These spectrophotometry techniques were used for filtered samples both from MER/O of natural sediments of varying masses with no added phosphate and for sorption experiments of natural and synthesized samples with varying initially added phosphate concentrations. To analyze SRP, we used the Malachite Green Assay [45] and to analyze for TDFe we used the Ferrozine Assay (Hach Method 8147). Calibration curves for both techniques were obtained from reference solutions of our PIPES buffer with reacted DQ or ABTS after filtration through the 0.2  $\mu\text{m}$  membrane filter. Solution SRF or TDFe concentration was calculated from the best linear fits of the calibration curves.

### 2.2.4 $\mu$ -X-ray Fluorescence (Multi-)Energy Mapping

$\mu$ -X-Ray Fluorescence ( $\mu$ -XRF) (multi-)energy mapping was used to map spatial distribution or relative abundance of Fe and P in mounted sediment samples. During the first round of beamtime we analyzed our natural MBS samples before and after reduction and oxidation via MER and MEO, respectively. The reduction sample of 186 mg and

oxidation sample of 192 mg MBS were subjected to MER and MEO, respectively, in our electrochemical cell, flash frozen with liquid nitrogen, and lyophilized prior to XAS analyses. All the samples were mounted on Kapton tape at the beamline, and the reduced sample was mounted within an anaerobic chamber to prevent re-oxidation of the sample. At beamline 2-3, we ran iron  $\mu$ -XRF maps of an approximate 2x2 mm area with a 5  $\mu$ m beam diameter and a 7  $\mu$ m step size, making each pixel on the map a 7x7  $\mu$ m area. Maps were obtained at 7150 eV, near the Fe k-edge energy. At beamline 14-3 we obtained  $\mu$ -XRF maps with the same beam size and step size settings, but with different areas and energies. Initially maps were taken at 2160 eV, near the P k-edge associated with phosphate species to map spatial distribution of relative abundance of phosphate. Based on the initial maps, we selected areas with multiple hotspots to take multi-energy maps over much smaller areas (due to time restrictions with scheduled beamtime) at energies 2147.7, 2149.0, 2152.0, 2152.15, 2152.3, 2152.5, 2155.0 eV. Some of these energies were very close together and didn't show significant variations in spatial distributions, so for further multi-energy maps we narrowed our selected energies.

During our second round of beamtime we wanted to increase our Fe and P concentrations and also evaluate distribution and speciation of P integrated with time. To increase the Fe and P concentrations we added known amount of ferrihydrite and goethite to our MBS samples and sorbed them with phosphate solution for 24 hours, like in the first step of the sorption experiments. We created four ~200 mg samples that were sorbed with 4 mL of 100 ppm phosphate for 24 hours: MBS with ~10% ferrihydrite, MBS with ~25% ferrihydrite, MBS with ~10% goethite, and MBS with ~25% goethite. The entirety of these samples was put into the anaerobic glovebox, reduced for 4-5 hours, flash frozen, and lyophilized before analysis. Samples were taken from each of the slurries with 10% synthesized mineral additions at time 0, 15 min, 30 min, 1 hr, and 4 hrs. Samples were taken from each of the slurries with 25% synthesized mineral additions at time 0, 15 min, 30 min, 1 hr, 2 hrs, and 5 hrs. All of these samples were mounted and  $\mu$ -XRF maps were obtained for each, except for the 25% ferrihydrite MBS sample from 2 hours, which got lost during sample transit. Multi-energy maps were taken for these samples simultaneously, as compared to previous beamtime where we took an initial map to select our smaller multi-energy areas, at beamline 2-3. Energies included 2147.7, 2149.0,

2152.0, 2155.0, and 2160.0 eV. The indications for each of these energies for types of phosphate species are included in Table 2.

| Energy (eV) | Phosphate Species Association                                    |
|-------------|--|
| 2147.7      | Pre-edge peak associated with Fe oxide sorbed $\text{PO}_4^{3-}$ |
| 2149.0      | Pre-edge peak associated with Fe oxide sorbed $\text{PO}_4^{3-}$ |
| 2152.0      | Main k-edge peak energy for phosphorus in phosphate              |
| 2155.0      | Post-edge feature, typically for apatite species                 |
| 2160.0      | Post-edge interference energy for determining “total” phosphate  |

**Table 2.** Significance of Selected Energies for Phosphorus Multi-Energy Mapping.

### 2.2.5 X-Ray Absorption Near Edge Spectroscopy Analyses

Based on our  $\mu$ -XRF maps from beamline 2-3 for Fe and 14-3 for P we were able to select spots within samples to obtain x-ray absorption near edge spectroscopy (XANES) data. With our  $\mu$ -XRF maps we can determine *where* the iron and phosphorus are; however, the XANES spectra are necessary to determine *what* the iron and phosphorus are. For our initial reduced, untreated, and oxidized MBS samples we selected around 10 spots on our map. We ran quick principle component analyses (PCA) on maps to select grains that were representative of the diversity of Fe and P species in our samples. Most spectra were targeted at large grains with high Fe/P concentrations, but we also included a few targeted within the more diffuse background areas. Our XANES data were taken with a beam diameter of 5  $\mu\text{m}$ . For our time series integrated samples with added synthetic ferrihydrite, goethite, and sorbed phosphate we were able to obtain XANES spot data for some, but not all, samples due to beamline time constraints.

## 2.3 Results

### 2.3.1 Mediated Electrochemical Reduction and Oxidation of MBS Samples

MER and MEO were performed on MBS samples of 5 mg, 10 mg, 20 mg, and 30 mg in duplicate. These redox techniques were successful in driving redox reactions in

MBS slurries at neutral pH 7. Although samples of each mass were run in triplicate, and relative standard deviation for area under the curve for samples ranged from 0.87-15.85%, and so a 20% conservative error was applied to the resulting data due to variations in redox environment, such as oxygen and hydrogen concentration of the anaerobic chamber, for each MER/MEO scan. The area between these curves and the baseline value at zero  $\mu\text{A}$  represents the number of electrons exchanged between the electrode surface and electron transfer mediator species, with electrodes polarized at  $E = -0.65\text{ V}$  for MER and  $E = 0.55\text{ V}$  for MEO versus an Ag/AgCl reference electrode. As the mediators are at equilibrium with the polarized electrode when the samples are added, the signal during the second scan between the working electrode and mediator directly reflects any reaction taking place between the sample species and mediator in solution, as shown in Figure 5. Reduction reactions are shown in the positive current axis, while oxidation reactions are shown on the negative current axis. For this set of MBS data, a baseline value was made from the average current of the last 100 seconds of each scan and subtracted from the curve for calculating electron exchange capacity (EEC), more specifically electron accepting capacity (EAC) for reduction and electron donating capacity (EDC) for oxidation curves. The Base R package in R Studio was used for the baseline subtraction calculation and to integrate the area under the curve and calculate EEC for all baselined subtracted reactions. EEC resulting from each reaction is plotted in Figure 6 as a function of total mass of sediment added to the electrolytic cell. The drop in measured current apparent for the oxidized 30mg sample was caused by the cell's magnetic stirring battery shutting off before the scan was completed.

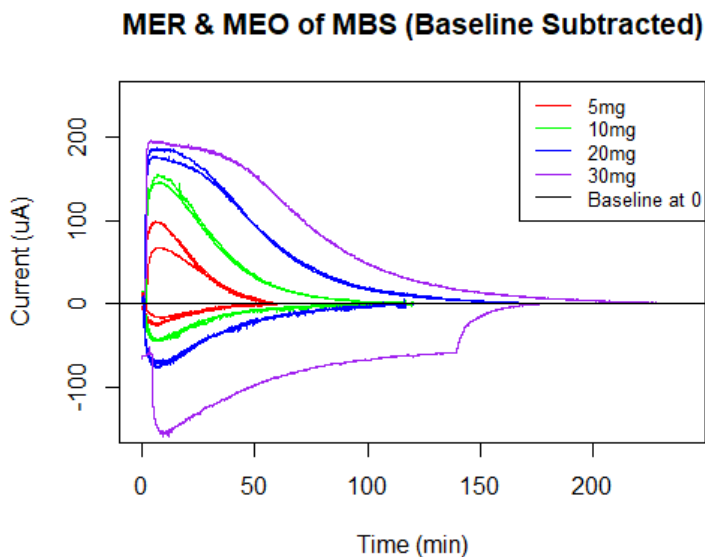


**Figure 5.** Chronoamperometric Curves for Reduction (Positive Current Axis) and Oxidation (Negative Current Axis) for Varying Masses of MBS in 3 mL of PIPES Buffer Solution. Each Curve Represents the Baseline Subtracted Reduction and Oxidation Curves for MBS Samples.

EAC is significantly higher than EDC for the MBS samples of the same mass. The number of moles of electrons exchanged between the sample and the working electrode (expressed in mmol) was calculated using Equation 1 and plotted in Figure 6. These values are based on averaged data from the EECs derived using curves shown in Figure 5, taken from the last 100 data points when the baseline became stable. For the oxidized 30 mg sample, the baseline average was taken before the current dropped to near zero. With increasing mass, there is a strong positive linear correlation with the number of moles of electrons exchanged in redox reaction. For all sample mass reactions, the number of electrons exchanged with the electrode surface were over 250% higher, and up to 340.43% as shown in the 5 mg sample, in reduction reactions than in oxidation reactions.

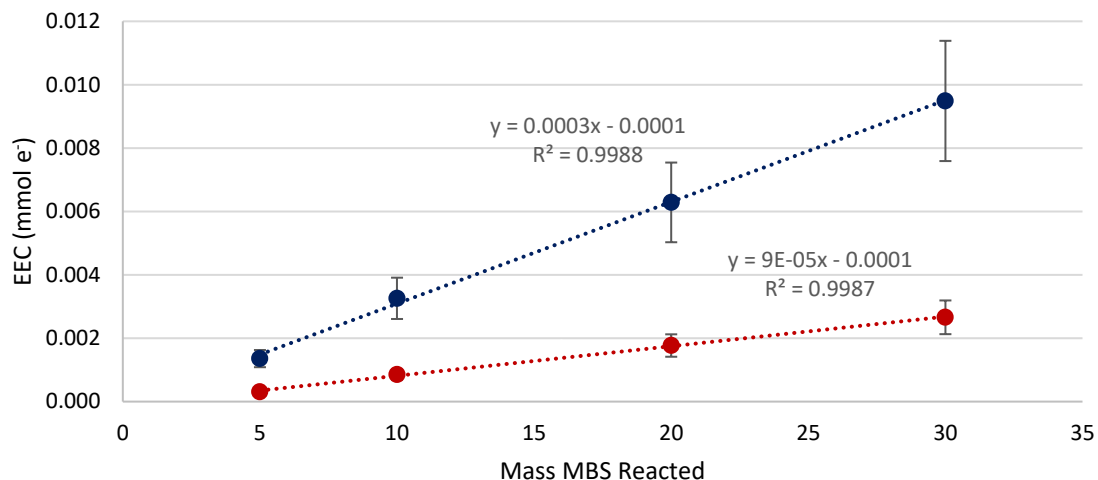


**Figure 6.** EEC of MER (Blue) and MEO (Red) Experiments Conducted on Varying Masses of MBS with 20% Standard Deviation.

### 2.3.2 Total Dissolved Iron and Soluble Reactive Phosphate from MBS

After MER and MEO experiments with MBS samples of masses 5-30 mg, we analyzed filtered solutions for SRP and TDFe, to determine the SRP and TDFe remaining in solution. This sample data represents released P and Fe from MER and MEO reactions of the pure MBS samples (no addition of sorbed phosphate). Oxidized samples showed low release of both SRP and TDFe, while reduced samples showed release of the existing solid fractions for both phases, with SRP concentrations below 413 ppb and TDFe concentrations below 107 ppb (Figure 7). Average TDFe concentration released after MER for these samples appears geochemically constrained (Figure 7B) with no linear relationship in released TDFe as a function of MBS mass reacted. With increasing sediment mass, released SRP after MER exhibits a continuous positive correlation (Figure 7A). Due to low concentrations of released SRP and TDFe from oxidized samples, further analyses were performed only with MER experiments, as these show to be more significant contributors to loss of solid phase SRP and Fe. When phosphate concentrations (0-50 ppm) were added to consistent mass of 100 mg MBS sediment, release of P increases for lower concentrations and is limited with higher concentrations of added phosphate (Figure 8A). Note the change in y-axis scale for these measurements. Released SRP from these samples increased with increasing starting concentrations of

phosphate up to 25 ppm; however not all phosphate is released into solution for samples with higher starting phosphate concentration and SRP concentrations level off and become consistent near 30 ppm for our samples that started with 25 and 50 ppm phosphate, suggesting geochemical limitations of SRP in solution after reduction of MBS samples with higher sorbed phosphate, or sorption of the phosphate to minerals that did not react as a result of MER. Released TDFe again remains relatively consistent for samples with relatively lower added phosphate (Figure 8B), and the concentration of TDFe released for our MBS samples with 50 ppm starting phosphate are lower than all other samples.

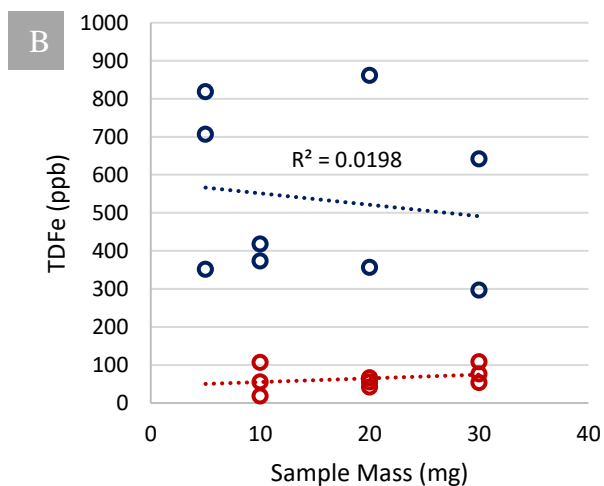
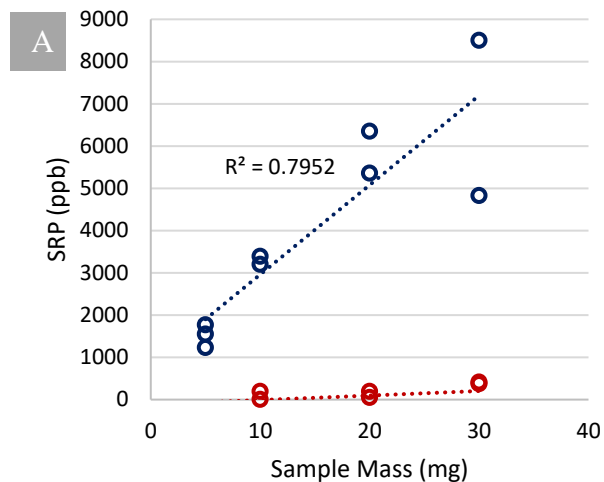


**Figure 7.** Plot of Released SRP (A) and TDFe (B) as a Function of Reacted MBS Sample Mass with No Added Phosphate. Red Data Points Represent Samples Analyzed After MEO and Blue Data Points Represent Samples Analyzed After MER.

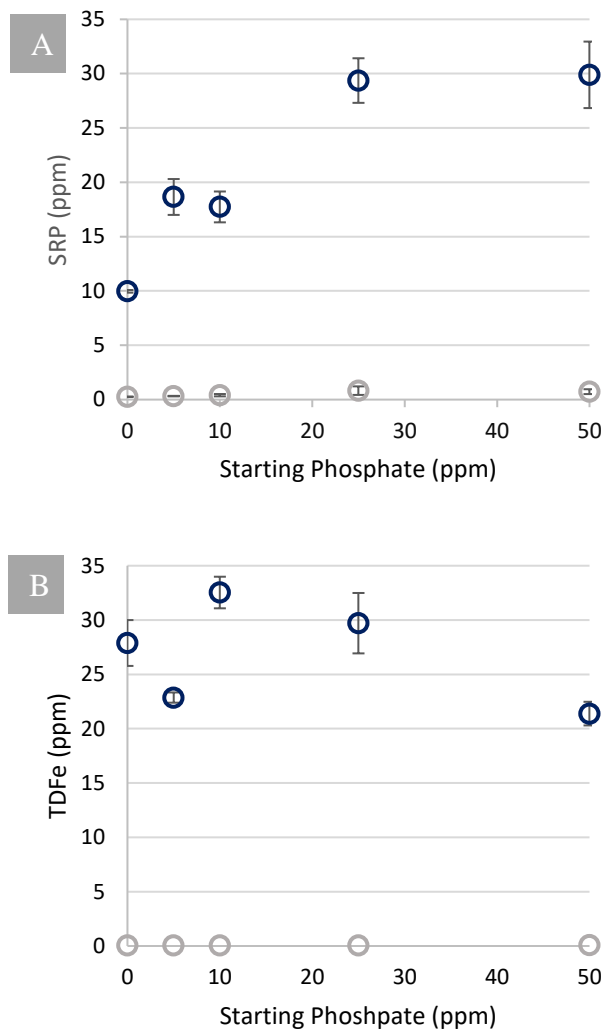


**Figure 8.** Plot of Released SRP (A) and TDFe (B) from 100 mg MBS Samples as a Function of Added Phosphate that was Sorbed for 24 hours in a Mixed Solution (Figure 3). Grey Data Points Represent the “After Sorption” Sample While Blue Data Points Represent the “After Reduction” Reduced Using MER. Standard Error is Represented as the Standard Deviation from Three Trials for Each Sample.

### 2.3.3 Mediated Electrochemical Reduction of Pure Mineral Samples

Pure mineral samples of 2-line ferrihydrite ( $(\text{Fe}^{3+})_2\text{O}_3 \cdot 0.5\text{H}_2\text{O}$ ) and goethite ( $(\text{Fe}^{3+})\text{O}(\text{OH})$ ) were reduced using the MER to evaluate rates and extents of reduction for each mineral using EAC and varying amounts of sorbed phosphate. Mineral composition and purity was confirmed by x-ray diffraction (XRD) analyses prior to MER

experiments. All samples were 5 mg of mineral standard mixed with varying concentrations of phosphate solution, from 0 ppm to 400 ppm for 24 hours. The chronoamperometric curves were baseline subtracted using R Studio to calculate mineral reduction extents. A conservative 20% error estimate was applied to the calculated percent of mineral reduced in Figure 9 to account for error associated with reduction conditions and baseline subtraction. This estimate again is based on error associated with the relative standard deviation from the MBS redox curves to account for variations in redox environment within the anaerobic chamber, for consistency of analyses. All ferrihydrite mineral samples reduced more completely than goethite samples, with overall reduction extents of 105 +/- 18.3% and 40.6 +/- 12.7% respectively. With a 90% confidence interval for both data sets, p-values for the ferrihydrite and goethite reduction extents versus phosphate concentrations were  $p=0.001$  and  $p=0.132$  respectively. These results suggest that phosphate concentration did not significantly affect the extent of goethite reduction, however phosphate concentration did significantly affect the extent of ferrihydrite reduction.

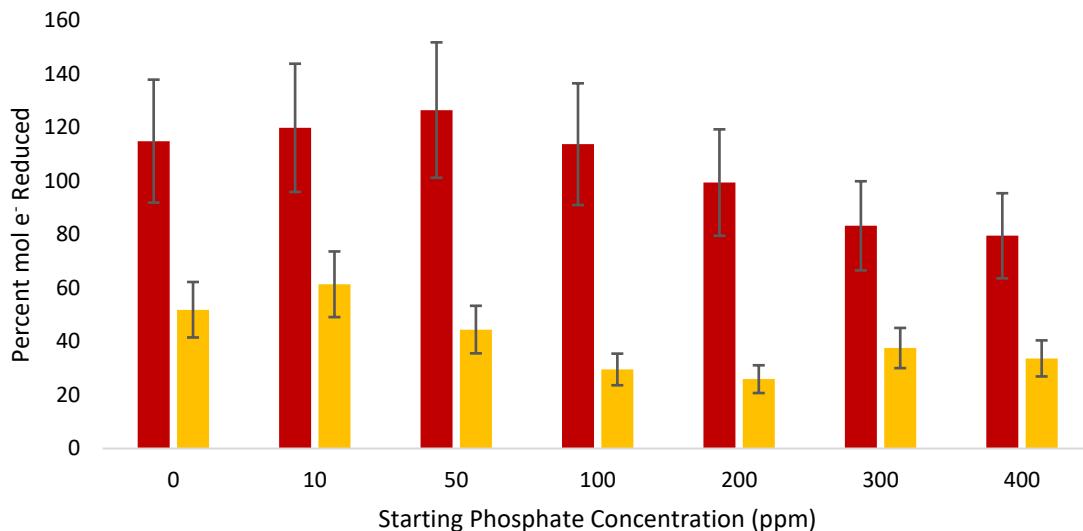


**Figure 9.** Mineral Reduction Extents from MER Curves for 5 mg Ferrihydrite (Red) and Goethite (Yellow) Samples with 20% Standard Deviation.

The rate constants ( $k$ ) for these reactions were calculated using equation 2:

$$\ln\left(\frac{C}{C_0}\right) = -kt$$

**Equation 2.** First order kinetics equation for calculating rate constants.

where  $C_0$  and  $C$  are initial and residual mineral concentrations, and  $t$  is time. The slope of the plots in Figure 10 represents the rate constant  $k$ . Samples FA-FG represent 5mg ferrihydrite samples with concentrations of starting phosphate 0, 10, 50, 100, 200, 300, and 400 ppm respectively. Samples GA-GG represent 5 mg of goethite samples with the same concentrations of starting phosphate concentration from 0-400 ppm. Data from sample GF was omitted due to an unstable ending baseline, inhibiting accuracy to calculate EAC and  $k$ . The linear logarithmic reduction of these samples exhibits first order kinetics at pH 7 with the working electrode polarized at -0.65 V. The rate constants and  $R^2$  values from the linear fits are listed in Table 3. Rate of reaction results are inconsistent with previous MER studies with these minerals [3, 36], however these studies involved pure mineral samples without added phosphate. Goethite samples reacted more quickly than ferrihydrite, although the extent of goethite reacted is more incomplete (Figure 9). Ferrihydrite reacted more completely but with more sluggish kinetics in comparison to the rates of goethite reduction. Although in Table 3 we can see that the rates of reduction were linear with all  $R^2$  values above 0.94. Regression analysis was performed to determine if the rate constants for ferrihydrite and goethite reduction reactions was significantly correlated to initial phosphate concentration of the solution. With a 90% confidence interval for both data sets, p-values for the ferrihydrite and goethite rate constants versus phosphate concentrations were  $p=0.058$  and  $p=0.896$  respectively. These results suggest that phosphate concentration did not significantly affect the rates of goethite reduction, however phosphate concentration did significantly affect the rates at which our ferrihydrite samples were reduced.

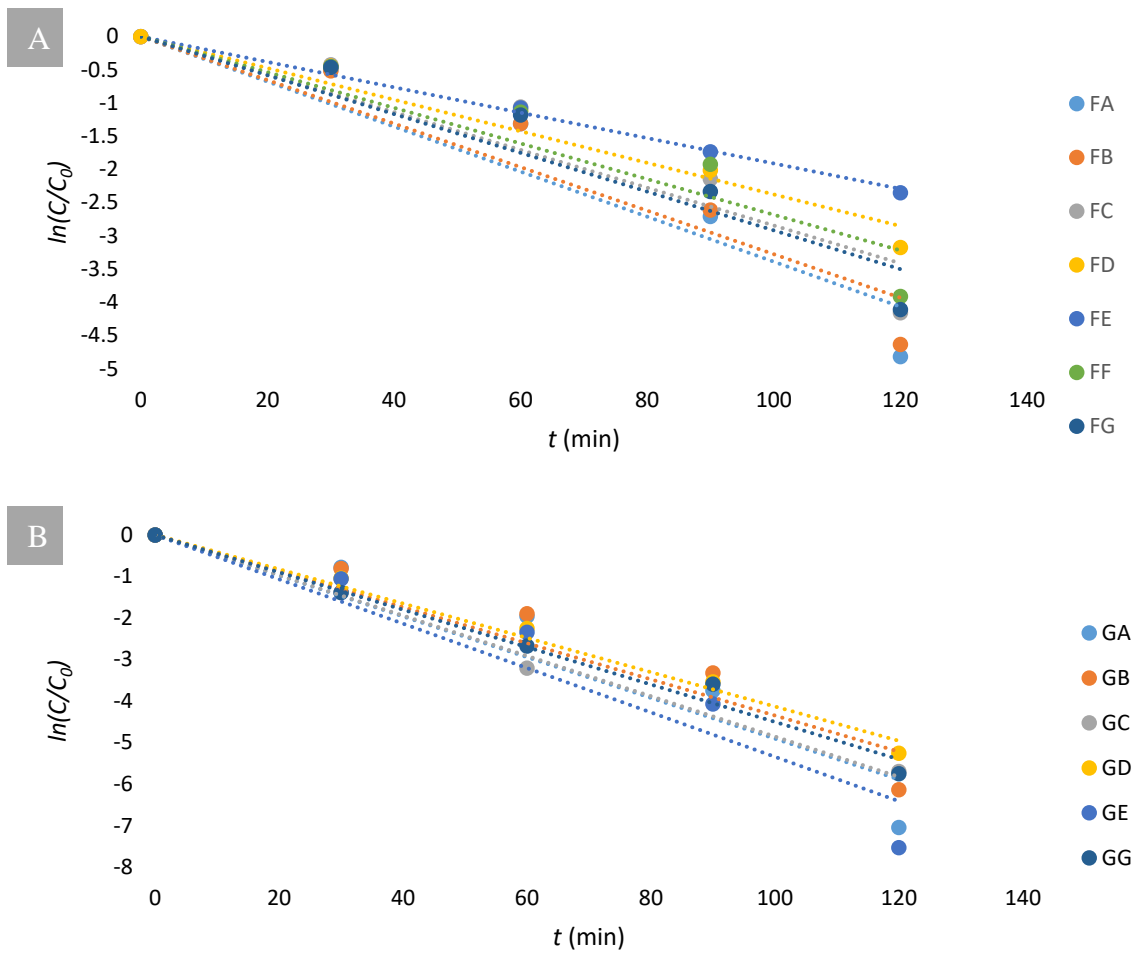


**Figure 10.** First-Order Rate Constant Plots for (A) Ferrihydrite Samples and (B) Goethite Samples with Sorbed Phosphate with Starting Concentrations from 0-400 ppm Phosphate.

| Starting Phosphate Concentration (ppm) | Ferrihydrite Samples |                | Goethite Samples |                |
|--|----------------------|----------------|------------------|----------------|
|  | $k$                  | R <sup>2</sup> | $k$              | R <sup>2</sup> |
| 0                                      | 0.034 +/- 0.0062     | 0.955          | 0.049 +/- 0.0094 | 0.953          |
| 10                                     | 0.033 +/- 0.0058     | 0.958          | 0.044 +/- 0.0074 | 0.963          |
| 50                                     | 0.028 +/- 0.0061     | 0.943          | 0.053 +/- 0.0026 | 0.0965         |
| 100                                    | 0.024 +/- 0.0027     | 0.981          | 0.041 +/- 0.0024 | 0.996          |
| 200                                    | 0.027 +/- 0.0007     | 0.948          | 0.053 +/- 0.0090 | 0.965          |
| 300                                    | 0.029 +/- 0.0056     | 0.960          | --               | --             |
| 400                                    | 0.019 +/- 0.0050     | 0.998          | 0.045 +/- 0.0035 | 0.994          |

**Table 3.** Rate Constants ( $k$ ) and Linear Fit R<sup>2</sup> Values for Reduction Rates of Pure 2-Line Ferrihydrite and Goethite Minerals Samples with Sorbed Phosphate.

#### 2.3.4 Total Dissolved Iron and Soluble Reactive Phosphate from Mineral Sorption Experiments

Sorption of phosphate from solution concentrations of 0-400 ppm to 5 mg of ferrihydrite or goethite resulted in depletion of nearly all phosphate from solution (Figure 11A and 12A). After sorption of phosphate to ferrihydrite for 24 hours, no Fe was released into solution for any sample, as shown in Figure 11A. Phosphate remaining in solution after 24 hours was limited, but not zero. After the sorption to ferrihydrite, SRP remaining in solution measured at 8.29 +/- 0.30 ppm SRP for all trials starting with 100 ppm or higher. After MER of these ferrihydrite samples with nearly all sorbed phosphate, Figure 11B shows the relationship between released SRP and TDFe in solution. TDFe concentrations gradually increase in samples with up to 100ppm starting phosphate and then drop off to near zero values. SRP concentrations are relatively low for low starting concentrations, and then increase respective to TDFe decreases beginning with our 100 ppm starting phosphate sample, shown in Figure 11B. The crossover point where SRP becomes higher than TDFe is at the 100 ppm starting phosphate sample. Although the starting phosphate concentration is increasing for these samples plotted along the x-axis, the starting Fe concentration is consistent across all of the ferrihydrite and goethite

samples weighing 5mg, suggesting that decreased concentrations of TDFe after reduction do not account for all of the Fe in the system. The released SRP for our ferrihydrite solutions remains relatively stable, averaging 32.20 +/- 2.60 ppm SRP for samples starting with 200, 300, and 400 ppm phosphate even though starting phosphate concentration were increasing. These results indicate that not all phosphate is accounted for in solution after reduction. Resulting released SRP and TDFe trends from goethite samples after sorption and after MER are similar to those observed with ferrihydrite samples (Figures 11 and 12). In Figures 11A and 12A it is apparent that no Fe was released into solution after sorption, and phosphate sorption is geochemically limited with 9.47 +/- 0.91 ppm SRP remaining in solution for both goethite and 2-line ferrihydrite. The sorption capacity for either mineral was not met with these sorption experiments, as a rise in SRP concentration after sorption would be expected. After MER of phosphate-sorbed goethite samples, SRP released remains relatively constant until an increase is seen beginning with our 100 ppm phosphate starting sample. The released SRP at higher starting concentrations levels off at 40.58 +/- 2.05 ppm SRP released into solution. Collectively, MER of the phosphate-sorbed goethite samples resulted in lower total percentages of mineral reduction than that of ferrihydrite (Fig 10B), and higher release of SRP and TDFe into solution after reduction, likely due to the lower molar mass of goethite meaning that more moles of Fe were present in these experiments. MER of phosphate-sorbed ferrihydrite samples resulted in near complete percentages of mineral reduction, moderate Fe release into solution for low starting phosphate concentration samples, <200 ppm, almost no released Fe into solution for samples  $\geq 200$  ppm, low SRP release into solution for low starting phosphate concentration samples, <200 ppm, and increased and relatively stable SRP release into solution for samples  $\geq 200$  ppm.

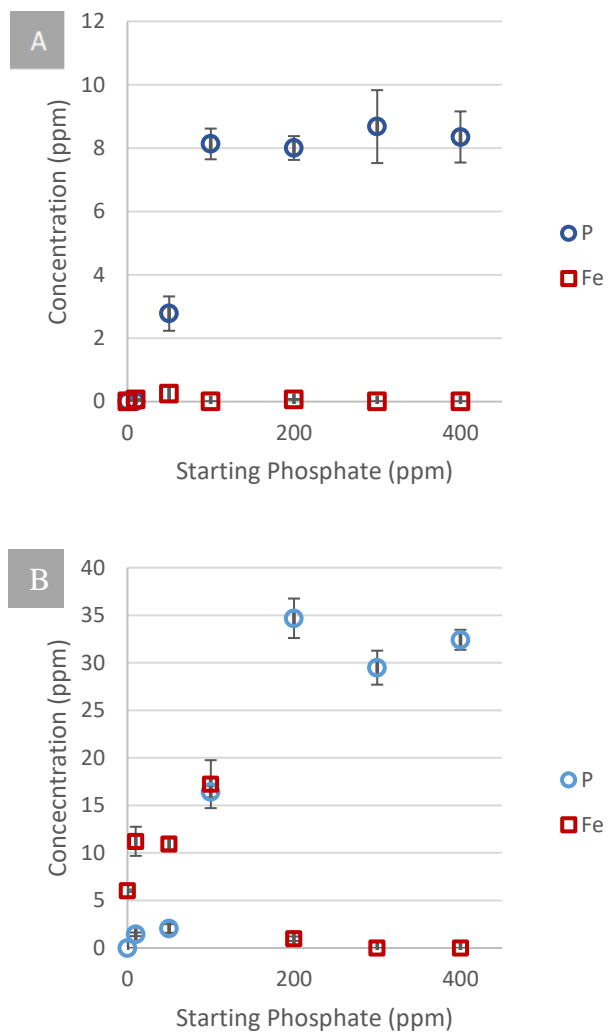


**Figure 11.** SRP and TDFe as a Function of Sorbed Phosphate After Sorption (A) and After Reduction (B) with 5 mg Samples of Pure 2-Line Ferrihydrite. Errors Bars Were Calculated Using the Standard Deviation of Three Absorbance Spectroscopy Samples for Each MER Trial.

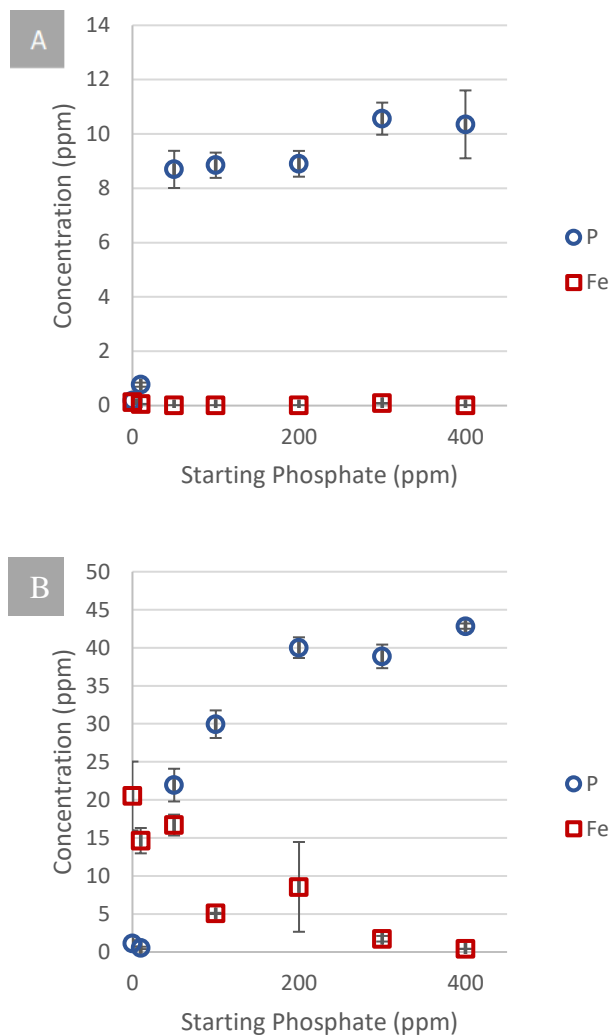


**Figure 12.** SRP and TDFe as a Function of Sorbed Phosphate After Sorption (A) and After Reduction (B) with 5 mg Samples of Pure Goethite. Errors Bars Were Calculated Using the Standard Deviation of Three Absorbance Spectroscopy Samples for Each MER Trial.

### 2.3.5 XAS Redox Experiments with MBS

To further analyze the geochemical changes concurrent with MER and MEO of MBS,  $\mu$ -XRF maps were obtained for three mounted sediment samples: MBS oxidized via MEO, an untreated sample of MBS, and MBS reduced via MER. The reduced and oxidized samples represent MBS after completion of redox changes. For Fe analysis,  $\mu$ -XRF maps were obtained at the Fe k-edge energy, 7150 eV to model relative abundance

and distribution of Fe in the sediment. XANES spots were selected based on these maps and obtained using a 5 micron diameter beam size. These maps are represented in Figures 13-15 with corresponding XANES spectra; general distribution of Fe is widely different across each image. In our untreated sample grains are much larger, however this may be attributed to lack of stirring time in solution prior to analysis. Large Fe-rich grains are more apparent in this sample, while small Fe-rich grains are present in the oxidized sample, and the reduced sample lacks large grains and areas heavily concentrated with Fe. The smaller, more Fe-rich grains in the oxidized sample may be due to break down of larger Fe grains, that retained their oxidized state while being stirred for 5 hours. Relative abundances of Fe in each map are scaled the same, making it apparent that the reduced MBS sample has relatively lower overall concentration of solid phase Fe in comparison to the oxidized and untreated MBS. This observation compliments the results shown in Figure 6B, where Fe was released and measured in solution samples after reduction of MBS rather than retained in the sediment sample. While these maps provide a robust analysis of Fe distribution within the sediment, the XANES spectra provides more intricate details about Fe-grain speciation across the maps.

Pre-edge peaks associated with Fe XANES spectra are typically attributed to Fe-phosphate minerals and Fe-minerals with sorbed phosphate. These pre-edge features are located between 7147-7149 eV, denoted by the arrow in Figure 13. Spectra numbers 1, 2, and 5 from the untreated MBS sample XANES have these pre-edge features (Fig 14). Spectra numbers 1 through 5 and 7 through 10 from the oxidized MBS sample XANES also have these features (Fig 13), while only 1, 2, and 10 from the reduced sample exhibit the pre-edge features (Fig 15), indicating that there are less Fe-P minerals or P-sorbed Fe minerals in our reduced sample that were identified via XANES as compared to the untreated and oxidized samples. With the exception of spectra 10, the large sediments grains from the untreated sample are representative of Fe minerals associated with P, with apparent gradient of high Fe concentration in the center of the grains that decreases with increasing distance from the center. The smaller grains within this sample do not have the pre-edge feature and are not complexed with P. All grains that were analyzed with XANES in the oxidized samples, with the exception of spectra 6, exhibit the Fe-P associated pre-edge peak regardless of relative grain size. Concentration gradients are

apparent in the oxidized sample Fe grains, as shown in Figure 13 in grains 1-3. Larger, more defined grains as well as diffuse grains, i.e. spectra 10, in the reduced sample have Fe-P complexed minerals, however the concentration gradient within the reduced sample is much less defined with centers less prominently concentrated with Fe.

In figures 16-18,  $\mu$ -XRF maps were obtained near the P k-edge energy, 2160 eV to observe changes in distribution and relative abundance of P for an untreated, oxidized, and raw sample of MBS. Pre-edge peaks in our P XANES spectra, between 2147-2149 eV are typically associated with Fe-P minerals and P sorbed with Fe minerals. A distinct post-edge 'shoulder' feature near 2155 eV is indicative of apatite mineral species. Since our motivation is to characterize Fe and P interactions in space and time, apatite minerals that were present are minimally discussed. Our untreated sample is similar to the  $\mu$ -XRF map obtained near the Fe k-edge in that it shows large P-depleted areas around the map, likely due to lack of stirring the sediment in solution and mechanical breakdown of mineral grains. Due to low signal to noise ratio, sample spectra in this sample were difficult to normalize to a baseline value. Our single XANES spectra in the untreated sediment sample does not contain our pre-edge feature and is not a P phase associated with Fe mineral sorption or apatite minerals. In the oxidized sediment sample, we see evidence of Fe-P minerals and P-sorbed Fe minerals for samples 1 and 2 which exhibit the pre-edge feature, while samples 3 and 4 are apatite grains. Sample spectra 1 and 6 from the reduced sediment sample display pre-edge features. While similar in size, spectra 1 has an apparent P concentration gradient that is increased towards the center of the grain while spectra 6 has a more constant P concentration throughout.

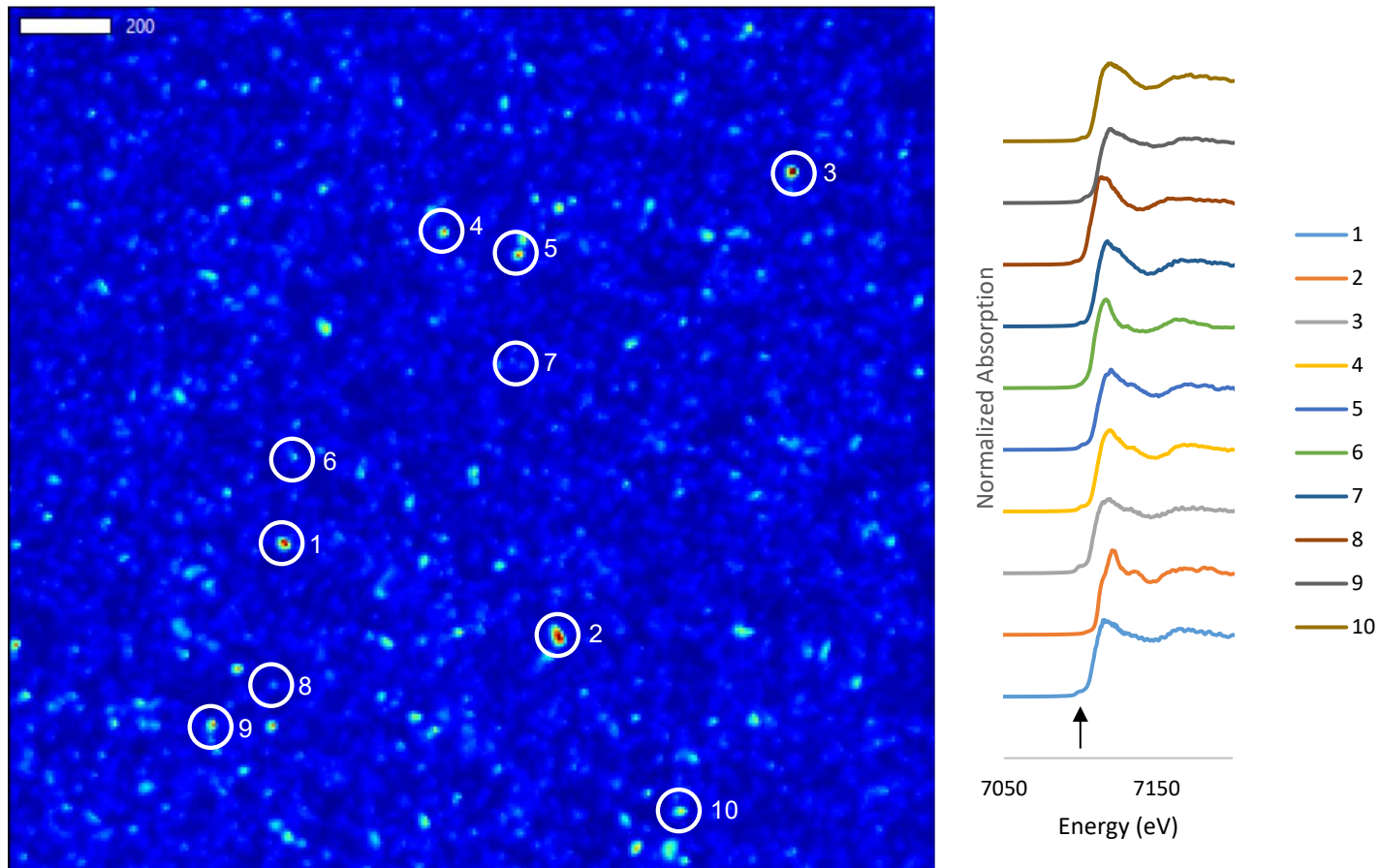


**Figure 13.**  $\mu$ -XRF Map of an Oxidized Sample of MBS Sediment Near the Fe k-Edge Energy, 7150 eV, and XANES Data Corresponding to Sediment Grains Indicated by the Plot Markers. The Scale Bar Represents 200 Microns.

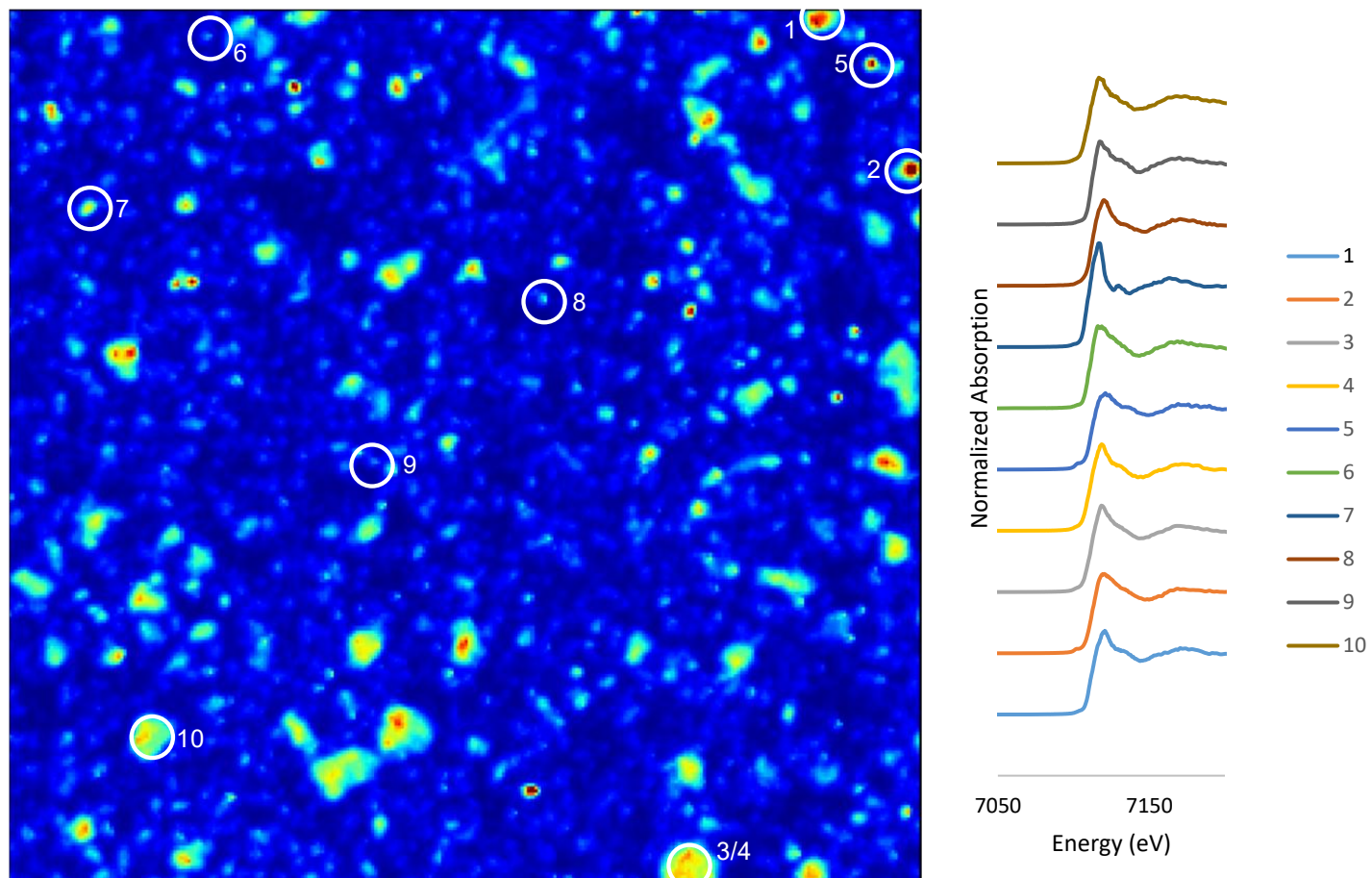


**Figure 14.**  $\mu$ -XRF Map of a Untreated Sample of MBS Sediment Near the Fe k-Edge Energy, 7150 eV, and XANES Data Corresponding to Sediment Grains Indicated by the Plot Markers.

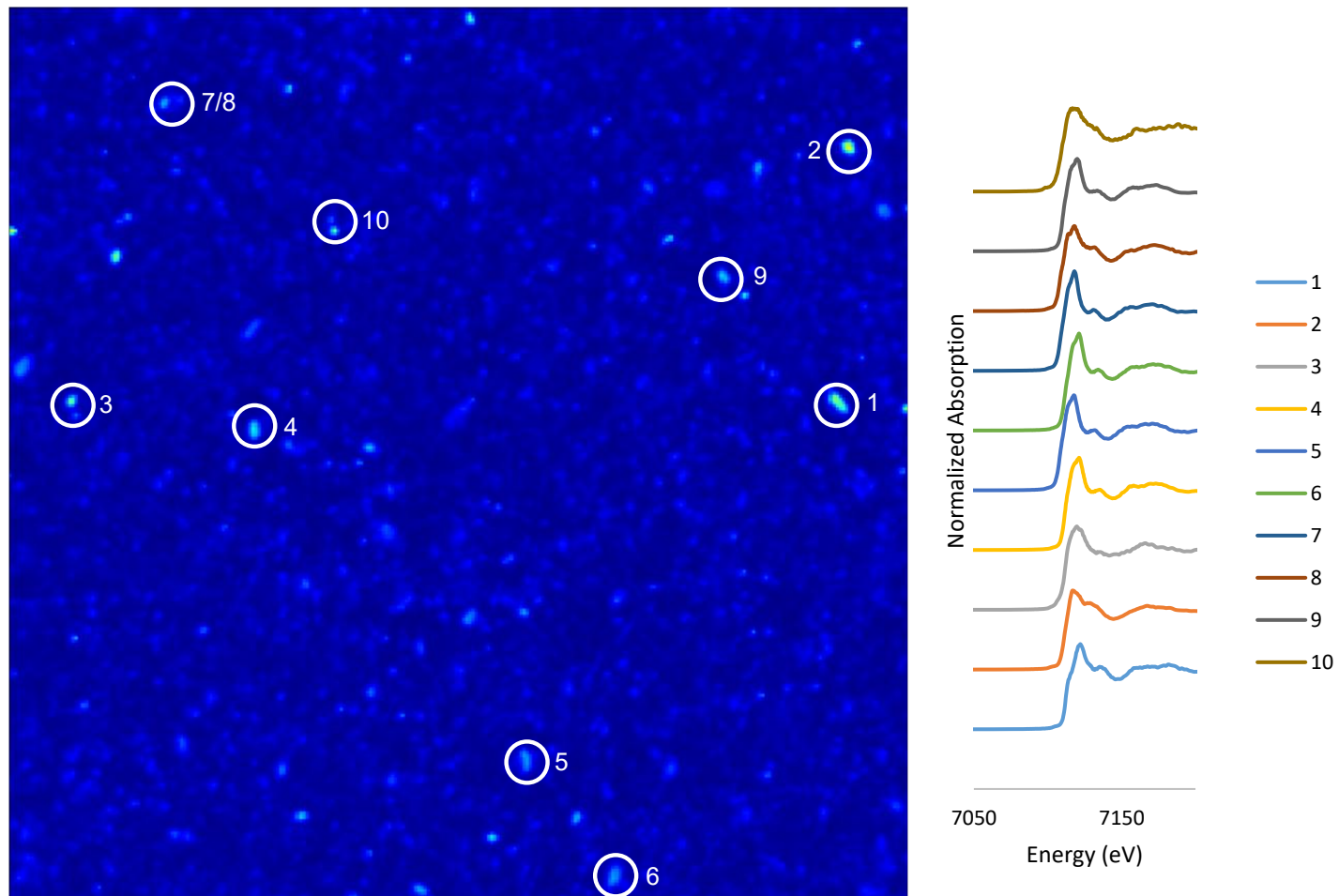


**Figure 15.**  $\mu$ -XRF Map of a Reduced Sample of MBS Sediment Near the Fe k-Edge Energy, 7150 eV, and XANES Data Corresponding to Sediment Grains Indicated by the Plot Markers.

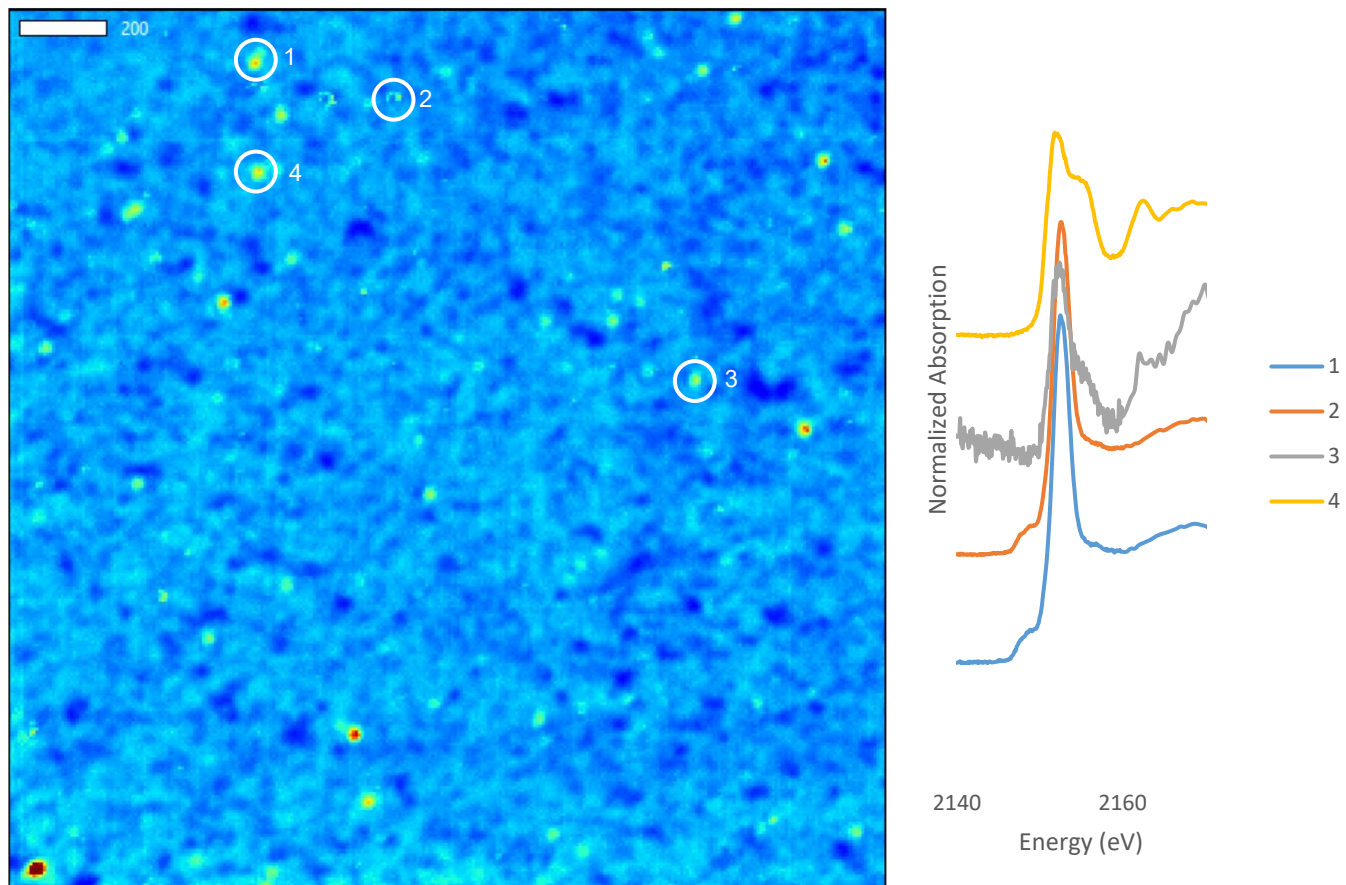


**Figure 16.**  $\mu$ -XRF Map of an Oxidized Sample of MBS Sediment Near the P k-Edge Energy, 2160 eV, and XANES Data Corresponding to Sediment Grains Indicated by the Plot Markers.

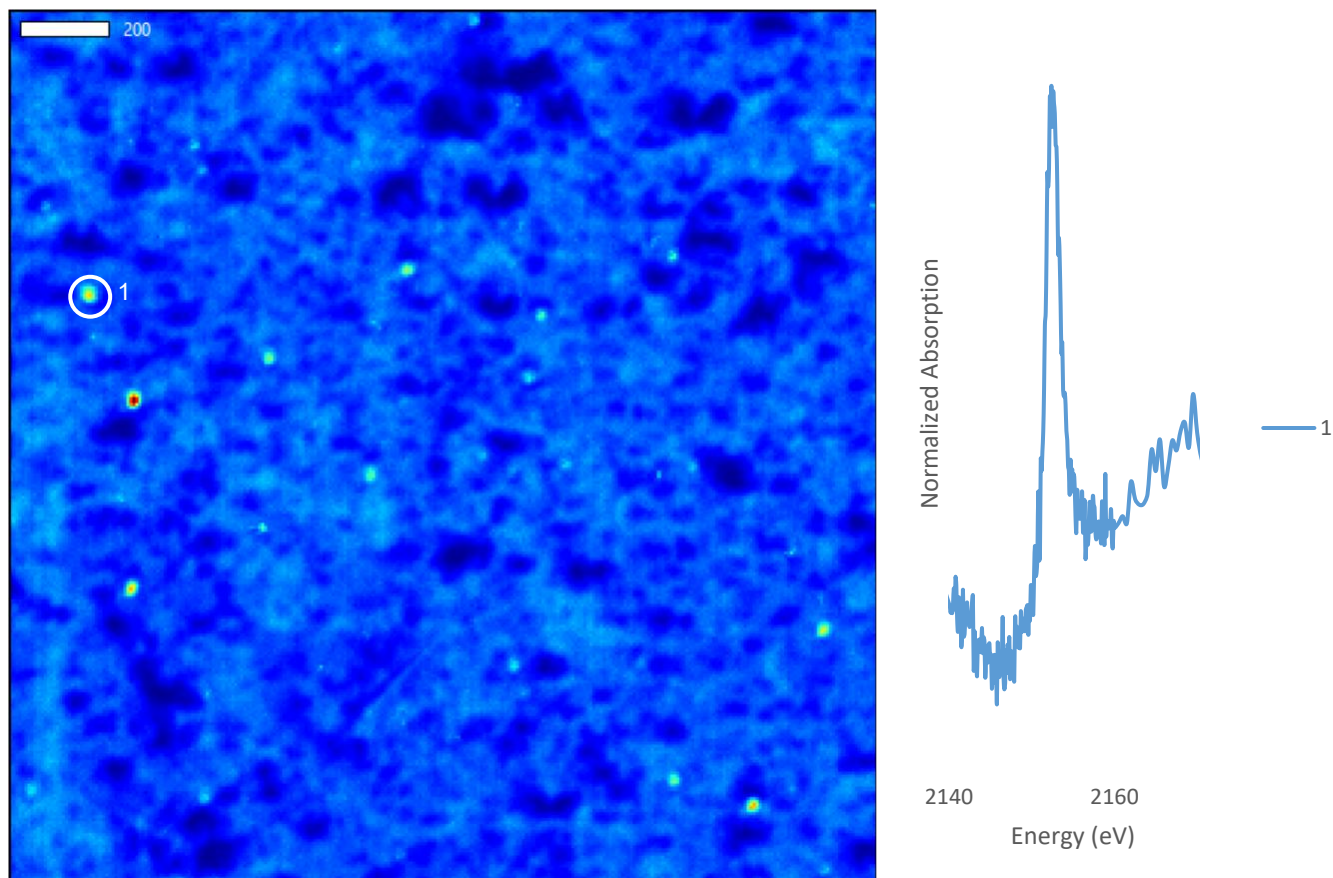


**Figure 17.**  $\mu$ -XRF Map of an Untreated Sample of MBS Sediment Near the P k-Edge Energy, 2160 eV, and XANES Data Corresponding to Sediment Grains Indicated by the Plot Markers.

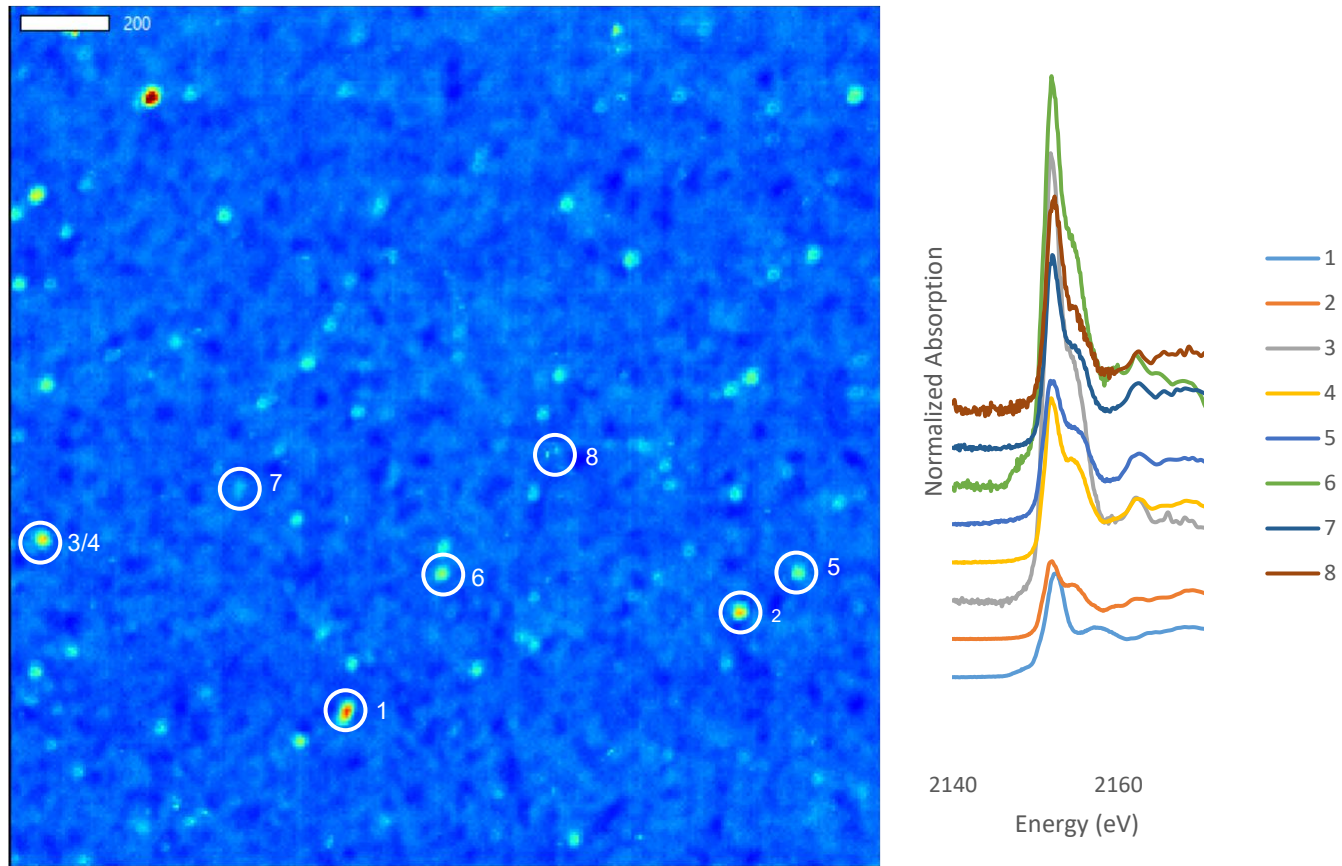


**Figure 18.**  $\mu$ -XRF Map of a Reduced Sample of MBS Sediment Near the P k-Edge Energy, 2160 eV, and XANES Data Corresponding to Sediment Grains Indicated by the Plot Markers.

### 2.3.6 XAS Time Series Experiments with Mineral Spiked MBS

Time series results portray  $\mu$ -XRF maps and corresponding XANES spectra during specific points throughout the redox processes driven by MEO and MER. Our samples for the time series experiments, shown in Figures 19 and 20, are representative of P distribution and speciation as a function of time with the times in minutes displayed above each sample  $\mu$ -XRF map. XANES spectra for points the sample maps are displayed in the corresponding plots below. The same methods were used to obtain the time series  $\mu$ -XRF maps, however the figures shown and tricolor plots representing three different energies with red, green, and blue. The red data points represent absorbance at 2147 eV, or P areas that are associated with Fe minerals. This component has been upscaled to 5 times that of the other two energies plotted, as the pre-edge feature at this energy is a much lower absorbance than the main K-edge peaks, as seen in the previous P XANES spectra. The green data points represent the P K-edge energy at 2152 eV, mapping P generally around the map. The blue data points represent post-edge features associated with apatite minerals at 2155 eV.

In the MBS-ferrihydrite mixture it is P abundance throughout the solid phase, represented in the maps, decreased as MER continues and increases again at the end. Although we would expect to see more red as the time of MER continues, the Fe associated P is only distinct in a single large grain after 300 minutes. Many of the grains that were analyzed via XANES are plotted more heavily in the K-edge feature and the post-edge apatite feature. Many spectra are discernable P with no significant pre- or post-edges features to determine mineral structure or are apatite, shown by the large post-edge shoulders in spectra 1-3 from the 15-minutes map and 5-2 through 5-5 in the 300 minute map. The MBS goethite maps were analyzed using the same color-energy correspondence. Almost all spectra, aside from the 300 minute 5-3 are variations of apatite. Red data points are less visible in the 300 minute end member map after equilibration was reached with MER. Relative abundance of P in the solid phase for these samples was increased before reduction, and relatively similar with increase in time reduced.

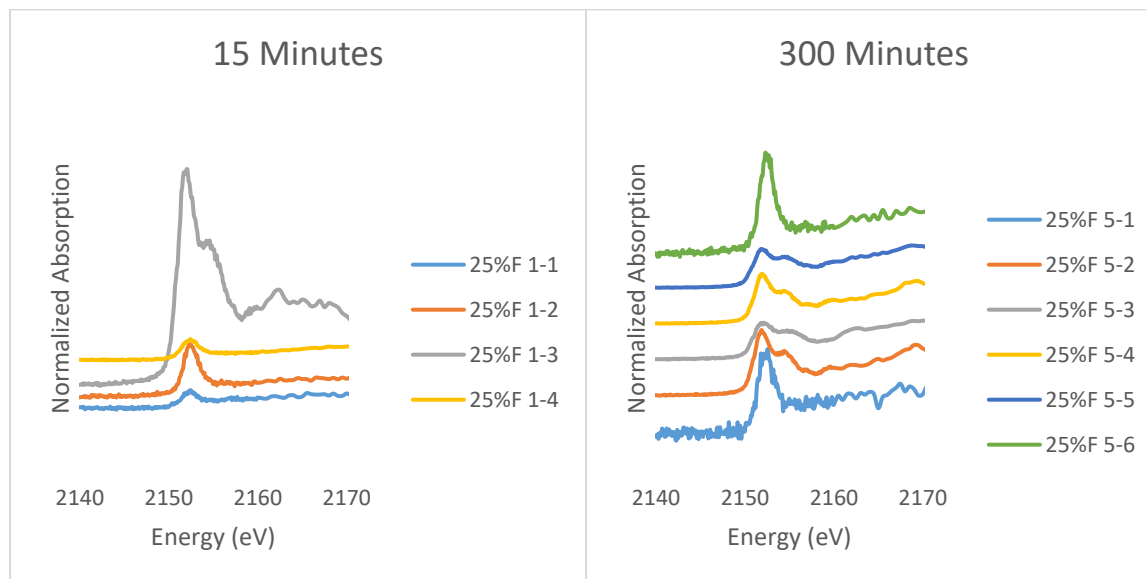
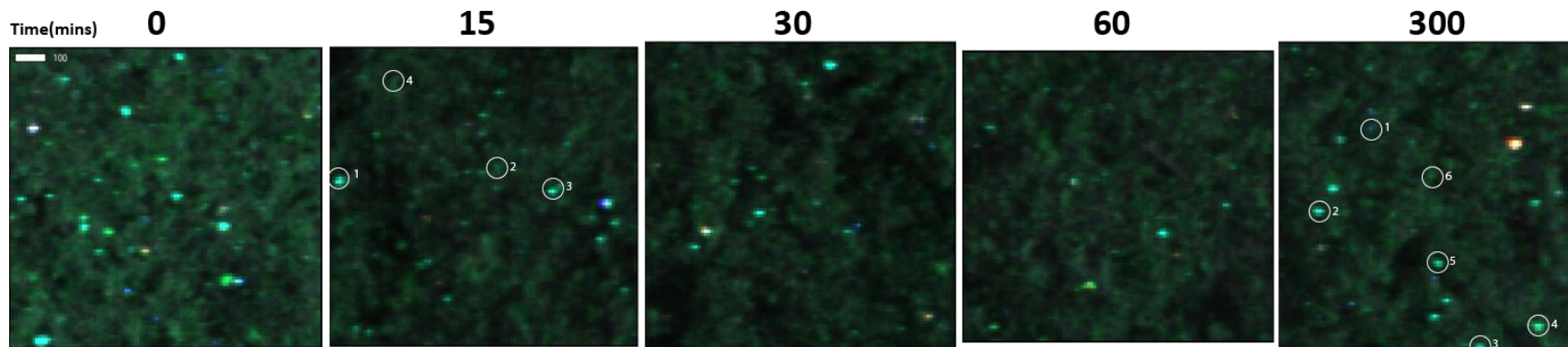


**Figure 19.** Time Series  $\mu$ -XRF Maps from a Sample of MBS with 25% Ferrihydrite Added After Times 0, 15, 30, 60, and 300 Minutes with Corresponding XANES Spectra.

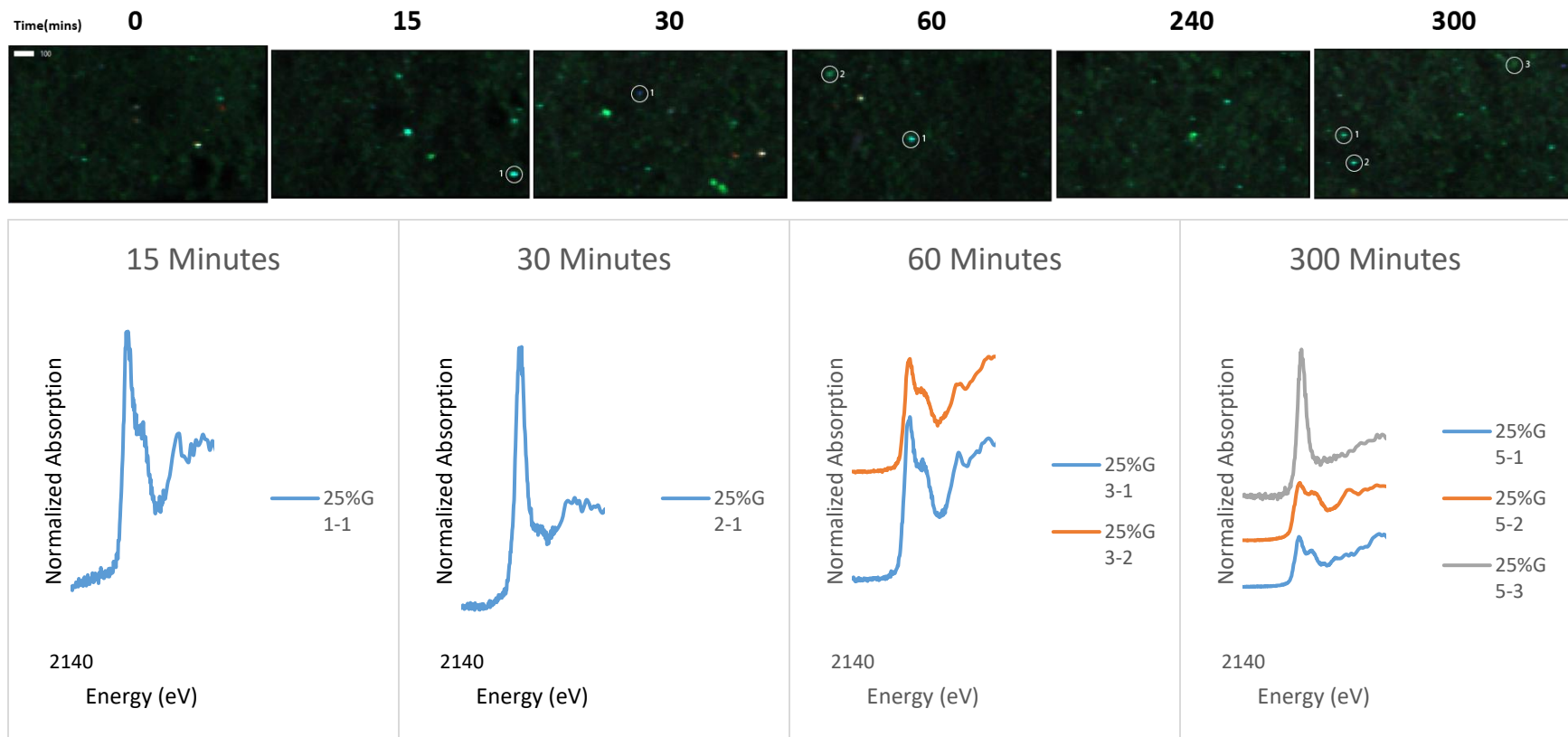


**Figure 20.** Time Series  $\mu$ -XRF Maps from a Sample of MBS with 25% Goethite Added After Times 0, 15, 30, 60, 240, and 300 Minutes with Corresponding XANES Spectra.

## 2.4 Discussion

### *2.4.1 Missisquoi Bay Sediment Redox Properties and Fe/P Cycling*

Missisquoi Bay of Lake Champlain (Vermont, USA) serves as a model for shallow, freshwater lake systems exhibiting significant P cycling and flux associated with redox changes from diel to annual time scales [31, 32, 34, 35]. This environment is extensively researched, and characterizations of Fe and P flux between water and sediment rely heavily on wind events, temperature, and watershed connection, all of which influence the redox behavior at the sediment-water interface that drives oxidative precipitation and reductive dissolution of Fe and P mineral phases [26, 31, 34]. Fe oxide minerals precipitate, ripen, and age over time as oxic environments persist [11] while Fe oxide minerals reduce and dissolve to release ferrous Fe to the water column in anoxic environments [36]. Oxidation and precipitation of Fe oxides occurs during unstable hydrodynamic conditions and oxygen penetration reaches further depths in the water column and reacts with ferrous Fe to initially create amorphous and small-grained Fe oxide minerals that readily sorb available P in the form of orthophosphate. Reductive dissolution of Fe minerals and release of P from surface sediments to water is observed during stable hydrodynamic conditions, and is magnified by cyanobacterial blooms where heterotrophic metabolisms consume oxygen more rapidly beneath the surface layer and deplete oxygen lower in the water column [32]. The samples that we have obtained from Missisquoi Bay are sediment samples from the top 5 cm of the sediment column that have been flash frozen, lyophilized, and sieved to 63  $\mu\text{m}$ . The MBS samples used in our experiments are representative of sediment with critical involvement in P transport in two specific ways: 1) the samples represent sediment that resides at the sediment water interface and are more susceptible than samples deeper in the sediment column to redox cycling between sediment and solution, and 2) the samples are fine-grained, and with more surface area sediment grains are more physically susceptible to geochemical changes in their environment, and thus coupled P cycling driven by redox transformations.

In the presence of oxygen, Fe oxide minerals precipitate in a sequence beginning with amorphous or nanoparticulate particles that are unstable, namely ferrihydrite. As

oxidation persists, ferrihydrite minerals begin to ripen, forming larger, more stable mineral structures and evolve into more stable Fe oxide minerals like goethite. In shorter time scales, oxidation of these smaller, more unstable mineral crystals promotes P sorption as these minerals exhibit both increased surface area and affinity for P sorption. Ferrihydrite has the highest sorption affinity of all Fe oxide minerals due to characteristics including poor crystallinity and high surface site density [46] and can retain more P in solid form, isolating P from the aqueous environment as it adheres to the solid mineral grains. As minerals ripen into more stable and larger-grained Fe oxides, affinity for P sorption decreases for minerals like goethite, as sorption affinity for phosphate continues decrease exponentially with increasing grain size of more stable Fe oxides [30]. When oxygen is depleted near the sediment water interface due to previously mentioned mechanisms such as stable hydrodynamic conditions and lack of water column mixing, Fe oxides reductively dissolve, concurrently releasing P as the mineral grains break down. The smaller, unstable and poorly crystalline minerals are the first to dissolve and release increased amount of P sorbed to their surface. As reductive mechanisms continue, more stable minerals, with focus on goethite, dissolve more slowly and incompletely. Even more stable Fe oxide minerals, such as hematite, are less critical in the coupled Fe/P cycling mechanisms as they have a much lower affinity for sorbing P and exhibit redox changes in time scales ranging from weeks to months. As reductive dissolution occurs and Fe and P are release into solution, saturation of these materials in the aqueous phase can lead to precipitation of new Fe-P minerals, such as vivianite with Fe(II) or strengite with Fe(III). Precipitation of these minerals reduces bioavailable P in the water column. Mediated electrochemical experiments serve as an electron transfer driver to understand the geochemical changes driven by redox changes for pure sediment samples, 2-line ferrihydrite, and goethite samples and observe rates and extents of reduction and oxidation in their isolated environments. These mediated experiments can indicate both the rates and extents of redox transformations of samples, and with coupled analyses can provide insights to specific geochemical changes in the system resulting from driven redox transformations. To understand how dissolved P in the water column further affects Fe and P cycling and redox dynamics, phosphate was also added to these samples via sorption before MEO and MER experiments.

Mediated electrochemical experiments were successful in driving redox reactions of MBS without the addition of phosphate (Figure 5) at pH 7 with an  $E_H^{\text{MER}}$  of -0.65 V and an  $E_H^{\text{MEO}}$  of 0.55 V. In these experiments, we hypothesized that MEO would oxidize largely organic molecules, including organic P molecules which make up a significant portion of P in these sediments [32], while MER would reduce Fe-oxide minerals in a sequence dictated by mineral stability, where ferrihydrite minerals are dissolved initially follow by goethite and more crystalline forms [3]. For MBS samples, MEO and MER extents of our sediment proportionally increased with increasing sediment mass from 5-30 mg (Figure 6) with the given system conditions, so we expect that extrapolating the trend would account for EEC estimates of larger amounts of sediment given the same system conditions in natural environments. Oxidation extents were much lower than reduction extents; however, MEO does drive reactions beyond those mitigated by exposure to the atmosphere over time, resulting in further oxidation of species within the MBS sample that can be thought of as possible metabolic reactions. Driven oxidation did not result in any significant release of Fe or P, as shown in Figure 7, which remained below 110 ppb (Fig. 7B) and 420 ppb (Fig 7A) even with our largest sample with 30 mg of oxidized sediment. This is consistent with studies claiming that during unstable hydrodynamic conditions and absence of algal blooms consuming large fractions of available oxygen, where oxygen penetration into the water column increases, presence of dissolved Fe and P is relatively lower and precipitation of Fe minerals and sorption of P to those Fe minerals occurs, even if additional bioavailable P (as orthophosphate for example) is released via microbial or mineral catalyzed dephosphorylation [47].

Reduction extents, and corresponding electron exchange capacity (EEC) between the working electrode and electron transfer mediator, displayed for all MER and MEO experiments in Figure 6, were more than twice that of the oxidation extents of MEO experiments for the same sediment mass. The gap between EEC continues to increase with increasing sediment mass. As mentioned previously, the MBS sample is representative of sediment that has been exposed to atmospheric oxygen over time and thus is readily susceptible to geochemical changes induced by MER-driven reduction and is readily 'reducible'. When reduced, MBS samples release both Fe and P, per Figure 7, indicating that reductive dissolution of Fe oxides and concurrent release of P sorbed to

these minerals within the MBS sample may occur on brief time scales ranging minutes to hours with significant reaction driving force, or reduced free energy. No specific trend with respect to Fe release from samples due to reduction of MBS via MER shown in Figure 7B is apparent as the aqueous Fe remains relatively constant from 5 to 30 mg of sediment reacted ( $R^2=0.0198$ ), while released P shown in Figure 7A continues to increase with increasing sample mass ( $R^2=0.7952$ ). This data suggests that with our concentrations of P, <9 ppm, and concentrations of Fe, <1 ppm after reduction, precipitation of Fe-P minerals in solution was minimal, if any, as decreases in the released concentrations of both Fe and P would be expected with new Fe-P mineral precipitation as reacted sediment mass increases. To observe changes in system mineralogy, coupled techniques are required in conjunction with the mediated electrochemical experiments, and thus  $\mu$ -XRF mapping and corresponding XANES data provided insights to elemental distribution and geochemical speciation of minerals across the sediment maps.

The initial batch of  $\mu$ -XRF mapping and corresponding XANES data aimed to characterize geochemical changes in Fe and P mineral forms as a result of oxidation and reduction driven by mediated electrochemical experiments for MBS samples without addition of P. Data presented in Figures 13-18 are Fe and P maps of oxidized, untreated, and reduced MBS samples mounted on a sample stage via sulfur-free tape and mylar without additional Fe oxide minerals or added phosphate from sorption experiments.  $\mu$ -XRF maps near the k-edge energy for Fe in Figures 13-15 show changes in Fe distribution in the samples between the oxidized, untreated, and reduced samples. Oxidized Fe minerals typically exhibit pre-edge peak features around 7097-7100 eV. The untreated MBS samples in Figure 14 exhibit both oxidized Fe minerals with pre-edge features and Fe minerals lacking pre-edge features. Data targeting large grains, including spectra 1, 2, 5, 7, and 10 are representative of oxidized Fe minerals, indicating that high portions of our large grains have likely ripened over time and concentrate in larger grains in surface sediments. The more diffuse areas, represented by all the other spectra within the sample, are a mixture of both oxidized and reduced Fe minerals. Nearly all oxidized MBS XANES in Figure 13 portray oxidized Fe minerals, in both the concentrated grains, such as spectra 2, and the diffuse areas, such as spectra 7 and 8. The spectra from this sample were analyzed via linear combination fitting (LCF) against our ferrihydrite and

goethite standards, as those are the two oxidized mineral species of focus given our time scales of further oxidation from MEO. All XANES spectra except for spectra 1 from the oxidized sample were fitted more closely to the goethite standard spectra, while there were more spectra similar to ferrihydrite in the untreated sample. This increased similarity of the oxidized sample to goethite not observed in the spectra obtained from the untreated sample XANES spots, with representative data presented in Table 4 and 5 below, suggesting that our oxidation driven by MEO experiments resulted in further ripening of existing ferrihydrite, or other Fe minerals, within the MBS sample into the more stable goethite mineral grains.

| Sample          | Ferrihydrite | Goethite |
|-----------------|--------------|----------|
| Oxidized MBS 1  | 88.0%        | 12.0%    |
| Oxidized MBS 2  | 10.0%        | 90.0%    |
| Oxidized MBS 3  | 15.7%        | 84.3%    |
| Oxidized MBS 4  | 7.5%         | 92.5%    |
| Oxidized MBS 5  | 11.3%        | 88.7%    |
| Oxidized MBS 6  | 5.2%         | 94.8%    |
| Oxidized MBS 7  | 3.0%         | 97.0%    |
| Oxidized MBS 8  | 0.0%         | 100.0%   |
| Oxidized MBS 9  | 0.0%         | 100.0%   |
| Oxidized MBS 10 | 0.0%         | 100.0%   |

**Table 4.** Linear Combination Fitting Results Fitted to Ferrihydrite and Goethite Standards from XANES Spectra Taken for the Oxidized Sample of MBS.

| Sample           | Ferrihydrite | Goethite |
|------------------|--------------|----------|
| Untreated MBS 1  | 86.6%        | 13.4%    |
| Untreated MBS 2  | 95.8%        | 4.2%     |
| Untreated MBS 3  | 43.2%        | 56.8%    |
| Untreated MBS 4  | 20.1%        | 79.9%    |
| Untreated MBS 5  | 97.7%        | 2.3%     |
| Untreated MBS 6  | 17.2%        | 82.8%    |
| Untreated MBS 7  | 0.0%         | 100.0%   |
| Untreated MBS 8  | 0.0%         | 100.0%   |
| Untreated MBS 9  | 0.0%         | 100.0%   |
| Untreated MBS 10 | 0.0%         | 100.0%   |

**Table 5.** Linear Combination Fitting Results Fitted to Ferrihydrite and Goethite Standards from XANES Spectra Taken for the Untreated Sample of MBS.

Reduction of MBS sediments results in XANES spectra across the sample that were depleted in oxidized Fe minerals, hence the lack of the pre-edge feature on the Fe XANES within the sample. Fitting these spectra with respect to vivianite and strengite would allow for differentiation of our suspected Fe-P mineral precipitates that occurred as a result of reduction and resulting solution chemistry. However, we did not have standards for these minerals and thus assumptions of mineral precipitation are reliant on the lack of pre-edge peaks observed in our reduced samples and aqueous solution chemistry trends from spectrophotometry experiments. We also induce that from the amounts of EAC exhibited by the reduction curves associated with MER experiments from these samples that reductive equilibrium was reached prior to XAS analyses coupled with lack of pre-edge features, reduced forms of FE minerals are dominant within this sample.

Our phosphorus XANES spectra taken across the maps obtained in Figures 16-18 display a higher, and unfavorable, signal to noise ratio making it difficult to discern different species of phosphorus at the untreated, oxidized, and reduced end member samples. Due to this data collection, we developed a new hypothesis that if we increased the concentration of phosphate in the samples for subsequent XANES spectra, then these

would be more likely to compare to our standards library of phosphate(-sorbed) minerals. Reduction experiments with phosphate added to MBS sediments did not occur until after the initial batch of XAS data. Our next approach was to add both phosphate, and ferrihydrite and goethite minerals, to the MBS samples and obtain more samples throughout the reduction process rather than just at reductive equilibrium, hence providing insight to more specific reaction mechanisms occurring during MER. Discussion from further XAS experiments are described in the next section.

#### *2.4.2 Iron Mineral Redox Properties and Fe/P Cycling*

Definitive trends in Fe and P speciation as a result of redox transformations were variable from initial experiments as there are more redox sensitive chemical components in the MBS sediment than just Fe minerals. To focus further on mechanisms specific Fe and P mineral species, further experiments with P sorption to MBS samples required the addition of raw Fe minerals to isolate transformations between the solid and aqueous phases resulting from reduction, oxidation, or lack thereof. Varying amounts of phosphate, from 0 to 50 ppm, were mixed in solution with MBS for 24 hours, and as shown by the grey data points in Figure 8 nearly all phosphate in solution was sorbed to the sediment and no Fe was present into solution after the equilibration time, and thus we did not exceed phosphate sorption capacity for these sediments up to 50 ppm of added phosphate for a 100 mg sample of MBS. Sequentially, the P-sorbed sediment samples were subjected to MEO and MER. The MEO results from the phosphate sorbed sediment are similar to the pure MBS sample data initially collected in that near zero amounts of Fe or P were present in solution after driven oxidation. For this reason, oxidation experiments were no longer performed, and the rest of the research focuses on the trends in Fe and P observed after reduction of all samples by MER. The phosphate-sorbed MBS samples after reduction exhibit inverse relationships in Fe and P release at higher concentrations of initially sorbed phosphate, shown by the blue data points in Figure 8. Trends in released Fe concentration begin to decrease with reduction of the 10 mg sample and released P concentration begins to decrease with reduction the 10 mg sample, suggesting that these components may be precipitating as mineral phases at higher concentrations of released phosphate. Research from Voegelin et al [2] found that when

aqueous ferrous Fe is oxidized in the presence of phosphate, that ferric Fe-P mineral precipitation is apparent at P:Fe ratios as much as ~0.16 and is the dominant phase produced at P:Fe ratios >0.55. The threshold for precipitation of ferrous Fe-P minerals as a result of reduction is not well characterized, especially in naturally occurring environments due to complex dynamic conditions and variability of water chemistry across lacustrine environments at the SWI in addition to likely fine-scale chemical heterogeneity across individual pore spaces. As reduction rates and extents of Fe-oxide minerals have been characterized by Aeppli et al [3, 36], we aimed to take experiments with pure Fe-oxide minerals, ferrihydrite and goethite, a step further by adding sorbed phosphate and observing the effects on both reduction rates and extents and redox-induced cycling between sediment and water. This also would help characterize the thresholds for ferrous Fe-P mineral precipitation theoretically resulting from reduction as a function of P:Fe ratios of the various samples of Fe-oxides with sorbed phosphate, in contrast to the previous studies focusing on oxidation reactions.

Ferrihydrite samples (5 mg) were sorbed with varying concentrations of phosphate from 0 to 400 ppb utilizing the same method and equilibration time as the P-sorbed MBS samples, for 24 hours. After equilibration for samples with more initial phosphate in solution, P remaining in solution reached a constant threshold near 8.29 ppm while almost no Fe was released from the fine-grained samples (Figure 11A). For the same mass goethite samples and same concentrations of phosphate added to solution the trend for P remaining in solution again established a threshold around 9.47 ppm with no Fe released into solution from the mineral sample (Figure 12A), concluding that for both minerals samples sorption continued until solution equilibrium with respect to phosphate concentration was reached. Even though ferrihydrite has a higher sorption affinity for phosphate than goethite [29, 46], with 5 mg of each sample and solution phosphate up to 400 ppb we did not exceed maximum sorption capacity for either Fe-oxide mineral.

The rates and extents of reduction of both the ferrihydrite and goethite minerals with and without sorbed phosphate are presented in Figures 9 and 10. Reduction extents of both minerals without added phosphate are consistent with previous findings that ferrihydrite reduces completely while goethite reduces incompletely at neutral pH. Some

ferrihydrate samples resulted in greater EEC than electrons present in the mineral sample, indicating that even with minimal oxygen concentration in the anaerobic chamber, ferrihydrate may be rapidly re-oxidized and available for reduction more than once within the 2-hour MER experiments. The addition of increasing amounts of phosphate up to 400 ppm appears to decrease the extents of reduction for both ferrihydrate and goethite, as the bar plots indicate a decrease in reduction extents at higher concentrations of phosphate in solution. Phosphate influence on reduction rates was different between the two Fe oxides. Both rate constants for ferrihydrate and goethite decrease with increasing phosphate concentration, according to Figure 10 and reduction rate constants Table 3. While both minerals exhibit decrease in reduction extents and rates with increasing phosphate concentration, phosphate only exhibits a significant effect on the reduction extents and rates of ferrihydrate reduction. Ferrihydrate's higher sorption affinity for P may explain why phosphate concentration inhibits the rate of electron transfer to the mineral grains, while the unchanging rate of goethite reduction results in release of lower P concentrations. It is possible that the sorption of phosphate onto the surface sites of the ferrihydrate minerals resulted in shielding from electron exchange with the electron transfer mediator, considering that previous studies conclude that ferrihydrate reduction is much faster than goethite reduction [36]. Increased phosphate on the surface of these small mineral grains could act as a barrier to delay reductive dissolution. In natural sediment systems, this could provide a hypothesis that increased legacy P adhered to more unstable Fe oxide minerals may increase the retainment of P in the solid phase and decrease aqueous bioavailability resulting from reductive conditions, at certain concentrations.

After reduction via MER for both the ferrihydrate and goethite samples with added phosphate, Fe concentration in solution decreased as sorbed phosphate concentrations increased, even with samples of the same mass. Phosphate release after reduction increased as initial phosphate concentration increased for both goethite and ferrihydrate, however in comparison to pre-experiment phosphate concentrations, some P was still unaccounted for in the aqueous phase and was retained in solid phase. This is due to either the retainment of phosphate within the mineral sediment or reductive dissolution and precipitation of new phosphate minerals. At lower concentrations of

initial phosphate, more Fe than P is released from the mineral sediments. SRP release becomes higher than Fe for samples above 100 ppm initial phosphate for goethite experiments (P:Fe = 0.075) and above 50 ppm for ferrihydrite experiments (P:Fe = 0.071). At 400 ppm initial phosphate, Fe in solution after reduction is zero or nearly zero for both minerals. The lack of correlation between aqueous P and Fe after reduction, coupled with the leveling concentrations of aqueous P concurrent with the decrease in aqueous Fe at higher initial P concentrations, suggests Fe and P mineral reprecipitation in these solution conditions. Precipitation of ferrous Fe-P minerals as a result of reductive dissolution of Ferric iron minerals with sorbed P would explain the trends in aqueous Fe and P concentrations that are inconsistent with previous data we collected. After reduction of MBS samples (Figure 7), concentration of released P continues to increase for all natural sediment samples. These results create a baseline for redox controlled release with concentrations of Fe and P lower than those for our latter experiments. While reduction of MBS caused continuous SRP release with increasing sediment mass, SRP release from reduction of P-sorbed Fe oxides did not continue to increase with increasing initial concentration of phosphate. The Fe concentration in solution is also orders of magnitude higher in the Fe oxide sediment slurries than in the MBS slurries, and the capability of ferrous Fe-P mineral precipitation is achievable in these conditions.

To achieve results more representative of natural sediments, while also increasing Fe and P concentration to create adequate conditions for probable ferrous Fe-P mineral precipitation after reduction, our second series of samples taken to the beamline for  $\mu$ -XRF mapping and XANES analyses were MBS sediments with 25% added ferrihydrite and goethite by weight, with 100ppm sorbed phosphate prior to reduction. We also took time series aliquots during total reduction times of 5 hours for the 25% ferrihydrite MBS sample and the 25% goethite sample with the goal of capturing specific geochemical changes between the natural and reduced state of the sediment on refined time scales, rather than just end member samples. The  $\mu$ -XRF maps for the 25% ferrihydrite sample in Figure 19 are presented as tricolor plots, where red is plotted as 2147 eV to represent pre-edge features of Fe-P minerals, green is plotted as 2152 eV to represent phosphate at the k-edge energy for phosphate P, and blue is plotted as 2155 eV to represent any apatite minerals exhibiting a post-edge shoulder. The red data point threshold for plotting

purposes was increase 10-fold, due to lower energy absorption at the pre-edge features in comparison to spectra characteristics as 2152 and 2155 eV.

For the 25% ferrihydrite sediment maps shown in Figure 19, initial maps show abundant P-rich grains prior to reduction with MER. Many of these are either representative of total phosphate at 2152 eV or the post-edge feature at 2155 eV indicating apatite species grains. A few grains also portray a mixture of the higher energy features with the 2147 eV pre-edge features, however the precise speciation of these potential Fe-associated P minerals is not known as we did not obtain XANES data from this map. Even lacking XANES spectra for all maps due to time constraints, it is clear that overall phosphate concentration in the solid phase decreased from 0 to 60 minutes of time subjected to MER as we see less and less grains apparent in the sample for all three plotted energies. XANES spectra from the 15 minutes samples show that spot F1-3, a larger grain on the map, was an apatite species due to its post-edge shoulder. The other spectra from this samples were a smaller grain (F1-1) and more diffuse areas, where our background to noise ratio was too high to discern pre- or post-edge features and identify characteristics of the P mineral present. At 300 minutes, four apatite minerals (F5-2 through 5-5) were captured through XANES analysis. Other specific species are difficult to distinguish as a low signal to noise ratio was still apparent for the diffuse areas within the sediment map. The sample at 5 hours does exhibit increased abundance of the red plotted grains, indicating that there are Fe-associated P minerals present after complete reduction of the ferrihydrite-mixed sediment sample that were not present in the initial, untreated sediment. These indicate that formation of new Fe-P minerals, such as vivianite, may have formed between phosphate and ferrous Fe that were released into solution as a result of MER.

Geochemical differentiation of species present in solution proved more difficult than expected, even with increased concentrations of Fe and P species of interest added to our MBS sediments. At such refined scales of mapping measured at 7  $\mu\text{m}$  resolution, the sediment samples were more homogeneous, and fine-grained, at this scale than expected. Lack of distinguishing ferrous Fe-P precipitates after reduction could have happened for several reasons. Firstly, it is possible that the mineral grains did not precipitate, however this is a highly unlikely scenario considering the trends in Fe and SRP solution

concentration after reduction as determined by our solution chemistry characterization. Secondly it is possible that the structure of these minerals may have resulted in inability to characterize via XANES because the surface of the precipitates had increased Fe or P relative to the center of the grains. Thirdly, and the most likely scenario for lack of the precipitates in the spectra and maps is that the grains were so small that even at microscopic resolution we were not able to see them. This is probable due to such quick reaction times preventing ripening of large precipitates, as well as constant stirring and convection of the system that did not allow more ripening of mineral grains to occur. Aside from difficulties with elemental mapping and XAS experiments, solution chemistry and trends in reduction extents and rates agree with the consensus that phosphate concentration has a closely coupled redox cycling mechanism with Fe oxides and may influence the redox properties and cycling of these minerals between solid and aqueous phases.

## CHAPTER THREE: CONCLUSIONS AND FUTURE DIRECTIONS

### 3.1 Conclusions and Reflection from Existing Research

Mediated electrochemical experiments are a reliable technique to drive redox reactions of not only single chemical species of interest but also more complex heterogenous samples such as those found in natural environments. While the redox transformations as a result of our MER and MEO experiments were successful and we can confirm that the answer to our first research question is yes, determining specific chemical transformation reactions and speciation of both solution and sediment are difficult with such fine-grained samples even with bulk solution chemistry and microscale elemental and speciation analyses. Results from our solution chemistry analyses favor the idea that prolonged reduction of Fe oxide minerals with P:Fe ratios above 0.71 for ferrihydrite and above 0.75 for goethite result in a change in release of Fe and P from the solid phase in a system isolated from other chemical species in sediments that could be explained by precipitation of Fe-P minerals like vivianite. With lack of specific identification of vivianite in the reduced samples from XANES analyses, further experiments are needed to confirm the presence and specific geochemical characterizations of these precipitates after MER driven reactions.

We also conclude that sorbed phosphate concentration influences the reduction rates and extents for ferrihydrite minerals, where higher concentrations of phosphate sorbed to these minerals inhibit mineral reduction extents and slows the reduction kinetics of ferrihydrite as compared to previous research. Our theory is that phosphate sorption to the surface of ferrihydrite minerals shields the grains from electron transfer between solution chemistry and reductants, however more refined analysis of the structure of specific minerals grains is needed to confirm this phenomenon. This correlation was not found with respect to reduction rates for goethite samples, as the more stable Fe oxide has less sorption capacity for phosphate and sorption of phosphate is less saturated on the mineral surfaces. Iron minerals do rely on phosphate interactions to influence their redox properties in isolated environments. Analyses of the chemical solutions require further experimentation to determine what is happening to the distribution of Fe and P during redox transformations in terms of geochemical pathways

and end members present after reduction reactions. We will rely on more intricate techniques of furthered research to confirm the geochemical fate of iron and phosphate in both isolated and natural systems. Although while phosphate does prove to be an environmental contaminant of interest in the aqueous, bioavailable form of orthophosphate, increased concentrations and sorption to minerals within sediments at high enough concentrations may inhibit reduction of readily reducible Fe oxides at the SWI and self-regulate as legacy phosphate continues to increase.

### 3.2 Future Needs

We did not achieve results as we expected for our XANES analyses with MBS sediments and Fe/P spiked sediments in terms of identifying dominant chemical species. We would have expected to see a higher abundance of samples representative of vivianite or other Fe-P minerals, potentially strengite in oxidized samples, after reductive dissolution with higher Fe oxide fractions in our solid samples. The state of the MER and MEO experiments was successful, as we know from our chronoamperometric curves that significant redox transformations were driven for all samples. For future endeavors,  $\mu$ -XRF maps may require smaller areas to more comprehensively analyze XANES spectra and comply with time restrictions that that arise with use of the beamline techniques. Mapping smaller areas would allow for more XANES spectra per map, however we have mentioned the homogeneity of the MBS samples at this scale and may sacrifice representation of the sediment as a population. Further XAS techniques along with alternative techniques, such as x-ray diffraction (XRD), are required to fully analyze the specific geochemical components of such small samples as these refined techniques are time consuming.

## REFERENCES

- Meret Aeppli, Andreas Voegelin, Christopher A. Gorski, Thomas B. Hofstetter, Michael Sander, *Mediated Electrochemical Reduction of Iron (Oxyhydr-)Oxides under Defined Thermodynamic Boundary Conditions*. Environmental Science and Technology, 2018. **52**: p. 560-570.
- Meret Aeppli, Ralf Kaegi, Ruben Kretzschmar, Andreas Voegelin, Thomas B. Hofstetter, Michael Sander, *Electrochemical Analysis of Changes in Iron Oxide Reducibility during Abiotic Ferrihydrite Transformation into Goethite and Magnetite*. Environmental Science and Technology, 2019. **53**: p. 3568-3578.
- Allen J. Bard, Larry R. Faulkner, *Electrochemical Methods*. 2nd ed. 2001: John Wiley & Sons, Inc.
- Jade J. Basinski, Sharon E. Bone, Annaleise R. Klein, Wiriya Thongsomboon, Valerie Mitchell, John T. Shukle, Gregory K. Druschel, Aaron Thompson, Ludmilla Aristilde, *Unraveling iron oxides as abiotic catalysts of organic phosphorus recycling in soil and sediment matrices*. Nature Communications, 2024. **15**: p. 1-14.
- Qin Boqiang, Yang Liuyan, Chen Feizhou, Zhu Guangwei, Zhang Lu, Chen Yiyu, *Mechanism and control of lake eutrophication*. Chinese Science Bulletin, 2006. **51**(19): p. 2401-2412.
- David J. Burdige, Tomoko Komada, *Iron redox cycling, sediment resuspension and the role of sediments in low oxygen environments as sources of iron to the water column*. Marine Chemistry, 2020. **223**.
- Michael F. Chislock, Enrique Doster, Rachel A. Zitomer, Alan E. Wilson, *Eutrophication: Causes, Consequences, and Controls in Aquatic Ecosystems*. Nature Education Knowledge, 2013. **4**(4): p. 10.
- Julie Cosmidis, Karim Benzerara, Guillaume Morin, Vincent Busigny, Oanez Lebeau, Didier Jezequal, Vincent Noel, Gabrielle Dublet, Guillaume Othmane, *Bio-mineralization of iron-phosphates in the water column of Lake Pavin (Massif Central, France)*. Geochimica et Cosmochimica Acta, 2014. **126**: p. 78-96.
- D'Angelo, E., Crutchfield J.; Vandiviere, M., *Rapid, sensitive, microscale determination of phosphate in water and soil*. J Environ Qual, 2001. **6**: p. 2206-2209.
- T. C. Daniel, A. N. Sharpley, J. L. Lemunyon, *Agricultural Phosphorus and Eutrophication: A Symposium Overview*. Journal of Environmental Quality, 1998. **27**: p. 251-257.
- Shiming Ding, Yan Wang, Dan Wang, Yang Yang Li, Mengdan Gong, Chaosheng Zhang, *In situ, high-resolution evidence for iron-coupled mobilization of phosphorus in sediments*. Scientific Reports, 2016: p. 1-11.
- G. M. Filippelli, *The Global Phosphorus Cycle: Past, Present, and Future*. Elements, 2008. **4**: p. 89-95.
- G. M. Filippelli, *The Global Phosphorus Cycle*. Reviews in Mineralogy and Geochemistry, 2002. **48**(1): p. 391-425.
- Courtney D. Giles, Peter D. F. Isles, Tom Manley, Yaoyang Xu, Gregory K. Druschel, Andrew W Schroth, *The mobility of phosphorus, iron, and manganese through the sediment-water continuum of a shallow eutrophic freshwater lake under stratified and mixed water-column conditions*. Biogeochemistry, 2015: p. 1-20.

- C. J. Gobler, *Climate Change and Harmful Algal Blooms: Insights and perspective*. Harmful Algae, 2020: p. 1-4.
- M. Haschke, U. Rossek, R. Tagle, U. Waldshlager, *Fast Elemental Mapping with Micro-XRF*. 2012: p. 286-298.
- Grant S. Henderson, Frank M. F. deGroot, Benjamin J. A. Moulton, *X-ray Absorption Near-Edge Structure (XANES) Spectroscopy*. Reviews in Mineralogy and Geochemistry, 2014. **78**: p. 75-138.
- Ellery D. Ingall, Jay A. Brandes, Julia M. Diaz, Martin D. de Jonge, David Paterson, Ian McNulty, W. Crawford Elliott, Paul Northrup, *Phosphorus K-edge XANES spectroscopy of mineral standards*. Journal of Synchrotron Radiation, 2011. **18**(2): p. 189-197.
- Peter D. F. Isles, Courtney D. Giles, Trevor A. Gearhart, Yaoyang Xu, Greg K. Druschel, Andrew W. Schroth, *Dynamic internal drivers of a historically severe cyanobacteria bloom in Lake Champlain revealed through comprehensive monitoring*. Journal of Great Lakes Research, 2015. **41**: p. 818-829.
- Deb P. Jaisi, Ravi K. Kukkadapu, Lisa M. Stout, Tamas Varga, Ruth E. Blake, *Biotic and Abiotic Pathways of Phosphorus Cycling in Minerals and Sediments: Insights from Oxygen Isotope Ratios in Phosphate*. 2011.
- Helen P. Jarvie, Colin Neal, Paul J. A. Withers, *Sewage-effluent phosphorus: A greater risk to river eutrophication than agricultural phosphorus?* Science of the Total Environment, 2005. **360**: p. 246-253.
- DongJoo Joung, Megan Leduc, Benjamin Ramcharitar, Yaoyang Xu, Peter D. F. Isles, Jason D. Stockwell, Gregory K. Druschel, Tom Manley, Andrew W. Schroth, *Winter weather and lake-watershed physical configuration drive phosphorus, iron and manganese dynamics in water and sediments of ice-covered lakes*. Limnology and Oceanography, 2017. **00**: p. 1-16.
- Jongsik Kim, Wei Li, Brian L. Philips, Claire P. Grey, *Phosphate adsorption on the iron oxyhydroxides goethite (a-FeOOH), akaganeite (b-FeOOH), and lepidocrocite (g-FeOOH): a 31P NMR Study†*. Energy and Environmental Science, 2011. **4**(10).
- Inho Namm, Jae Kyoo Lee, Hong Gil Nam, Richard N. Zare, *Abiotic production of sugar phosphates and uridine ribonucleoside in aqueous microdroplets*. PNAS, 2017. **114**(47).
- P. M. Nyenje, J. W. Foppen, S. Uhlenbrook, R. Kulabako, A. Muwanga, *Eutrophication and nutrient release in urban areas of sub-Saharan Africa - A review*. Science of the Total Environment, 2010. **408**: p. 447-455.
- Eric H. Oelkers, Eugenia Valsami-Jones, *Phosphate Mineral Reactivity and Global Sustainability*. Elements, 2008. **4**: p. 83-87.
- Chris T. Parsons, Fereidoun Rezanezhad, David W. O'Connell, Philippe Van Cappellen, *Sediment phosphorus speciation and mobility under dynamic redox conditions*. Biogeosciences, 2017. **14**: p. 3585-3602.
- J. G. Parsons, M. V. Aldrich, J. L. Gardea-Torresdey, *Environmental and Biological Applications of Extended X-Ray Absorption Fine Structure (EXAFS) and X-Ray Absorption Near Edge Structure (XANES) Spectroscopies*. Applied Spectroscopy Reviews, 2002. **37**(2): p. 187-222.

- Matthew A. Pasek, *Schreibersite on the early Earth: Scenarios for prebiotic phosphorylation*. *Geoscience Frontiers*, 2017. **8**: p. 329-335.
- Andrea R Pearce, Donna M. Rizzo, Mary C. Watzin, Gregory K. Druschel, *Unraveling Associations between Cyanobacteria Blooms and In-Lake Environmental Conditions in Missisquoi Bay, Lake Champlain, USA, Using a Modified Self-Organizing Map*. *Environmental Science and Technology*, 2013. **47**: p. 14267-14274.
- Michael Sander, Thomas B. Hofstetter, Christopher A. Gorski, *Electrochemical Analyses of Redox-Active Iron Minerals: A Review of Nonmediated and Mediated Approaches*. *Environmental Science and Technology*, 2015. **49**: p. 5862-5878.
- Donald Scavia, J. David Allan, Kristin K. Arend, Steven Bartell, Dmitry Beletsky, Nate S. Bosch, Stephen B. Brandt, Ruth D. Briland, Irem Daloglu, Joseph V. DePinto, David M. Dolan, Mary Anne Evans, Troy M. Farmer, Daisuke Goto, Haejin Han m, Tomas O. Höök, Roger Knight, Stuart A. Ludsin, Doran Mason, Anna M. Michalak, R. Peter Richards, James J. Roberts, Daniel K. Rucinski, Edward Rutherford, David J. Schwab, Timothy M. Sesterhenn, Hongyan Zhang, Yuntao Zhou, *Assessing and addressing the re-eutrophication of Lake Erie: Central basin hypoxia*. *Journal of Great Lakes Research*, 2014. **40**: p. 226-246.
- Andrew W. Schroth, Courtney D. Giles, Peter D. F. Isles, Yaoyang Xu, Zachary Perzan, Gregory K. Druschel, *Dynamic Coupling of Iron, Manganese, and Phosphorus Behavior in Water and Sediments of Shallow Ice-Covered Eutrophic Lakes*. *Environmental Science and Technology*, 2015. **49**: p. 9758-9767.
- Lydia Smith, Mary C. Watzin, Gregory K. Druschel, *Relating sediment phosphorus mobility to seasonal and diel redox fluctuations at the sediment-water interface in a eutrophic freshwater lake*. *Limnology and Oceanography*, 2011. **56**(6): p. 2251-2264.
- V. H. Smith, G. D. Tilman, J. C. Nekola, *Eutrophication: impacts of excess nutrient inputs on freshwater, marine, and terrestrial ecosystems*. *Environmental Pollution*, 1999. **100**: p. 179-196.
- Bryan M. Spears, Laurance Carvalho, Rupert Perkins, Alex Kirika, David M. Paterson, *Sediment phosphorus cycling in a large shallow lake: spatio-temporal variation in phosphorus pools and release*. *Hydrobiologica*, 2007. **584**: p. 37-48.
- Fatimah Sulu-Gambari, Dorina Seitaj, Thilo Behrends, Dipanjan Banerjee, Filip J. R. Meysman, Caroline P. Slomp, *Impact of cable bacteria on sedimentary iron and manganese dynamics in a seasonally-hypoxic marine basin*. *Geochimica et Cosmochimica Acta*, 2016. **192**: p. 49-69.
- Shigeru Suzuki, *Characterization of Formation of Ferrous and Ferric Oxides in Aqueous Solution from a Multidisciplinary Viewpoint*. *ISIJ International*, 2022. **62**(5): p. 800-810.
- William D. Taylor, David R. S. Lean, *Observations on the dynamics and fate of dissolved organic phosphorus in lake water and a new model of epilimnetic P cycling*. *Aquatic Sciences*, 2018. **80**(13): p. 1-9.
- Reyes Tirado, Michele Allsopp, *Phosphorus in agriculture: Problems and solutions*. *Greenpeace Research Laboratories Technical Report*, 2012: p. 1-35.

- Andreas Voegelin, Anna-Caterina Senn, Ralf Kaegi, Stephan J. Hug, Stefan Mangold, *Dynamic Fe-precipitate formation induced by Fe(II) oxidation in aerated phosphate-containing water*. *Geochimica et Cosmochimica Acta*, 2013. **117**: p. 216-231.
- Xiaoming Wang, Fan Liu, Wefeng Tan, Wei Li, Xionghan Heng, Donald L. Sparks, *Characteristics of Phosphate Adsorption-Desorption Onto Ferrihydrite: Comparison With Well-Crystalline Fe (Hydro)Oxides*. *Soil Science*, 2013. **178**(1): p. 1-11.
- Eugene B. Welch, G. Dennis Cook, *Internal Phosphorus Loading in Shallow Lakes: Importance and Control*. *Lake and Reservoir Management*, 2005. **21**(2): p. 209-217.
- F. H. Westheimer, *Why nature chose phosphates*. 1987. **235**: p. 1173-11178.
- Max Wilke, Francois Farges, Pierre-Emmanuel Petit, Gordon E. Brown Jr., Francois Martin, *Oxidation state and coordination of Fe in minerals: An Fe K-XANES spectroscopic study*. *American Mineralogist*, 2001. **86**: p. 714-730.
- Yunping Xu, Rudolf Jaffe, *Geochemical record of anthropogenic impacts on Lake Valencia, Venezuela*. *Applied Geochemistry*, 2009. **24**: p. 411-418.
- Jia-Zhong Zhang, Xiao-Lan Huang, *Relative Importance of Solid-Phase Phosphorus and Iron on the Sorption Behavior of Sediments*. *Environmental Science and Technology*, 2007. **41**: p. 2789-2795.

## CURRICULUM VITAE

Natalie A. Maag

### Education

- Master of Science in Geology  
Indiana University-Indianapolis (IUI)  
*May 2025*
- Bachelor of Science in Environmental Science  
Minors in Chemistry and Geochemistry  
Indiana University-Purdue University Indianapolis (IUPUI)  
*December 2020*

### Professional Experience

- Environmental Scientist  
Wessler Engineering | November 2023-Present
- Research Assistant  
Indiana University-Purdue University | August 2021-May 2023
- Research Assistant  
Indiana University-Purdue University | August 2021-May 2023
- Laboratory Technician Intern  
Patriot Engineering and Environmental | May 2021-August 2021

### Presentations

- Redox Include Cycling of Fe and P Near the Sediment Water Interface | Midwets Geobiology Symposium | September 2022
- Mediated Electrochemical Reduction: A Driver for Exploring Sediment-Water Cycling of Iron and Phosphorus | American Chemical Society Presentation | Indianapolis | March 2023